https://doi.org/10.5194/egusphere-2026-2541
Preprint. Discussion started: 12 June 2026

Validation of ITS_LIVE v2.0 mountain glacier velocities using in-situ GNSS data

Jing Zhang [1], Yang Lei [1,*], Laurane Charrier [2], Amaury Dehecq [2], Alex S. Gardner [3], Luke Copland [4], Christine Dow [5]

[1]National Space Science Center, Key Laboratory of Microwave Remote Sensing, Chinese Academy of Sciences, Beijing, China
[2]University Grenoble Alpes, IRD, CNRS, INRAE, Grenoble INP, IGE, Grenoble, France
[3]Jet Propulsion Laboratory, California Institute of Technology, Pasadena, USA
[4]Department of Geography, Environment and Geomatics, University of Ottawa, Ottawa, Canada
[5]Department of Geography and Environmental Management, University of Waterloo, Waterloo, Canada

Correspondence to: Yang Lei (leiyang@nssc.ac.cn)

Abstract. Glacier surface velocity is receiving increasing attention as it provides essential information on glacier dynamic processes, mass balance estimation, and glacier contributions to sea-level rise under global warming. Velocity products derived from satellite remote sensing have been widely applied to investigations of glacier surging dynamics, ice discharge quantification, and regional hydrological assessments. However, systematic in situ validation of satellite-derived velocity products over small mountain glaciers remains limited, with few studies providing comprehensive error assessment and uncertainty quantification. This gap hinders the reliable application of such products in regional glacier dynamic assessments and introduces unquantified uncertainties into downstream analyses, including mass balance estimation and ice discharge calculations. Here, we validate ITS_LIVE version 2 surface velocities derived from Sentinel-1, Sentinel-2, and Landsat-8 against in situ GNSS measurements over nine glaciers spanning three regions with contrasting dynamic regimes: the Yukon, Canada (fast-moving glaciers), the French Alps (narrow valley glaciers), and the Swiss Alps (slow-moving, small-scale glaciers). For the Yukon region, we validate ITS_LIVE image-pair time series against dense daily GNSS observations, applying two outlier removal strategies — error thresholding and spatial filtering — to improve data quality. For the European Alps, we validate both simple annual averages of ITS_LIVE image-pair products and ITS_LIVE annual composite products against annual-interval GNSS measurements. Regarding the validation results in the Yukon region, Sentinel-1 exhibits lower error in the range direction than in the azimuth direction, with the *vy* component (RMSE 9.4 m/yr, bias −1.7 m/yr) outperforming the *vx* component (RMSE 23.1 m/yr, bias 0.8 m/yr), reflecting the inherent anisotropy of SAR measurements. Among optical sensors, Landsat-8 exhibits lower spread (RMSE 16.3 m/yr, NMAD 4.3 m/yr) but higher systematic bias (3.7 m/yr), while Sentinel-2 shows greater spread (RMSE 22.4 m/yr, NMAD 9.6 m/yr) but negligible bias (−0.1 m/yr). Both optical sensors successfully detect the 2022 Lowell glacier surge event, with velocities exceeding 500 m/yr, demonstrating the capability of ITS_LIVE products to capture dynamic glacier flow events. Owing to its shorter repeat cycle, Sentinel-2 resolves finer temporal variability and retrieves higher surge velocities (>600 m/yr), though with increased uncertainty at shorter temporal baselines. As for the validation results in the European Alps, ITS_LIVE annual composite products are validated against annual-interval GNSS measurements. The annual composite products show lower bias (−1 m/yr in Switzerland and −29 m/yr in France) compared to simple annual averages of ITS_LIVE image-pair products (bias of 5–15 m/yr in Switzerland and −28 to 40 m/yr in France), demonstrating the effectiveness of the error-weighted least-squares fitting approach used in composite generation. Additionally, we validate the velocity errors provided with the ITS_LIVE products against GNSS–ITS_LIVE deviations and examine how velocity uncertainty evolves with image-pair time separation. Overall, the ITS_LIVE reported errors agree well with GNSS–ITS_LIVE deviations. This study bridges ground-truth observations with satellite-derived data, offering practical guidance on the applicable scope, expected accuracy, and noise removal strategies for ITS_LIVE v2 over small mountain glaciers.

1 Introduction

Glaciers are recognized as a significant factor in both contemporary (Zemp et al., 2019; Stringer et al., 2025) and projected sea level rise (Meier et al., 2007; Radic et al., 2014; Hock et al., 2019). As glaciers are sensitive to climate change, their dynamics play a crucial role in understanding glacier responses to changes in environmental forcing.

Glacier velocity is important for understanding the mass redistribution of glaciers and glacier contributions to oceans, which in-turn is important for improving projections of glacier change and their impact on water resources and sea level change (Minchew et al., 2017; Greene et al., 2020). Tracking features in repeated satellite imagery allows for the assessment of ice motion on continental scales. Surface velocities have been effectively obtained from both optical and radar imagery, including data from USGS's Landsat 4/5/7/8 (Fahnestock et al., 2016; Gardner et al., 2018; Zhang et al., 2020), ESA's Sentinel-1 (Nagler et al., 2015; Solgaard et al., 2021; Lei et al., 2022; Friedl et al., 2021), ESA's Sentinel-2 (Kaab et al., 2016; Millan et al., 2022; Troilo et al., 2024), and DLR's TerraSAR-X and TanDEM-X (Joughin et al., 2010).

The NASA Inter-mission Time Series of Land Ice Velocity and Elevation (ITS_LIVE) project (Gardner et al., 2025) provides satellite-derived glacier velocity measurements, constituting an invaluable resource for advancing our understanding of glacier flow and its temporal evolution at a global scale. The dataset delivers velocity observations for all glaciers and ice sheets larger than 5 km², and has been widely adopted across glaciological and ice-sheet research. ITS_LIVE underpins a broad range of applications. It has been used to detect glacier surges globally (Van Wychen et al., 2025), to characterize seasonal velocity variations (Greene et al., 2020), and when combined with velocity data, to estimate glacier mass balance (Zhou et al., 2022) and quantify ice-shelf calving losses in Antarctica (Greene et al., 2022). Beyond these direct applications, several studies have used ITS_LIVE as a benchmark for evaluating custom velocity-processing methods, including systematic comparisons with the CautoRIFT framework (Liu et al., 2024) and the generation of consistent velocity time series through the TICOI Python package (Charrier et al., 2025).

https://doi.org/10.5194/egusphere-2026-2541
Preprint. Discussion started: 12 June 2026

While several other global and regional ice velocity products exist, ITS_LIVE occupies a unique niche. For instance, the Programme for Monitoring of the Greenland Ice Sheet (PROMICE), which produces temporally averaged (24-day) velocity mosaics over the Greenland Ice Sheet using Sentinel-1 images; global products from Friedrich Alexander University (FAU), which provide feature image-pair products, as well as monthly and annual mosaics (Friedl et al., 2021); and global annual mosaics from Millan et al. (2022). The GoLIVE and FAU are constrained by their reliance on single sensors (Landsat-8 and Sentinel-1, respectively), limiting temporal density and data diversity. The multi-sensor dataset from Millan et al. (2019) overcomes the single-sensor issue but provides products only at annual resolution, restricting sub-annual analyses. ITS_LIVE combines a multi-sensor approach with a commitment to providing open-access, image-pair velocity granules, offering unparalleled opportunities for detailed time-series analysis and customized glaciological research.

The ITS_LIVE project releases a variety of products, including (1) image-pair velocity (without time averaging), (2) data cubes (time series of image-pair results), and (3) regional mosaics (temporally averaged), all of which deliver worldwide coverage through frequent, multi-sensor acquisitions combining optical (Landsat 4/5/7/8 and Sentinel-2) and SAR (Sentinel-1) satellite observations (Gardner et al., 2025). Landsat-based velocities cover the period from the mid-1980s to present, Sentinel-2 from 2015 to present, and Sentinel-1 from 2014 to present, provided as image-pair velocities and annual composites. Despite the wide adoption of ITS_LIVE products, there is a lack of in situ validation of ITS_LIVE product accuracy over small mountain glaciers. In this paper, we validate ITS_LIVE v2 glacier velocities by comparing image-pair and annual velocity mosaic products against in situ GNSS observations of ice flow across the Swiss Alps (where some GNSS points have nearest rock distances below 240 m), the French Alps (narrow valley glaciers) and the Yukon region (fast-moving glaciers). We compare ITS_LIVE v2 velocities from Sentinel-1, Sentinel-2, and Landsat-8 against these GNSS benchmarks, quantifying accuracy and assessing the magnitude and variability of platform-specific uncertainties. Finally, we discuss the factors that affect the ITS_LIVE product accuracy over small mountain glaciers.

2 Study Area

We selected three regions—the Swiss Alps, the French Alps, and the St. Elias Mountains in the Yukon, Canada—to span contrasting glacier regimes: slow-moving, narrow valley glaciers in France and Switzerland versus faster-moving systems in the Yukon (Zhang et al., 2024). Validation relies on in situ GNSS observations available in all three regions, using dense GNSS time series in the Yukon and annual-interval GNSS records in the Swiss and French Alps. The distances from the GNSS points to the glacier margins for the Yukon, France, and Switzerland are presented in Fig. S1, Fig. S2, and Fig. S3 of the supplementary materials, respectively.

2.1 Yukon region

The ice cover of the St. Elias Mountains spans 25,267 km² (Kienholz et al., 2015). Sevestre and Benn (2015) identified 322 surge-type glaciers, making the Alaska–Canada border region home to the world's third-largest concentration of such glaciers.

Glacier surges are quasi-periodic episodes of unusually fast ice flow, typically lasting from several months to several years (Bhambri et al., 2017; Cuffey and Paterson, 2010). Glacier flow instabilities occur across a wide continuum, with surge events representing the most severe manifestation of this phenomenon (Herreid and Truffer, 2016). The GNSS data used in this study were collected from three glaciers: Lowell, Kaskawulsh and Donjek (Fig. 1a).

The Kaskawulsh Glacier is approximately 70 km long, covers an area of 1,096 km² (Young et al., 2021) and consists of three main branches, referred to as the North, Central, and South Arms (Flowers et al., 2014). The glacier's North, Central, and South Arms originate in the Icefield Ranges at elevations of 2,578 m, 2,091 m, and 2,393 m a.s.l., respectively, and combine to flow eastward.

Lowell Glacier is an approximately 65-km-long surge-type glacier (Bevington and Copland, 2017). The last surge was reported in the winter of 2022-2023 (Van Wychen et al., 2023). Donjek Glacier is 55 km long and covered an area of 448 km² in 2010 (Abe et al., 2016). Its elevation ranges from approximately 1000 m a.s.l. at the terminus to over 3000 m a.s.l. in the accumulation area (Kochtitzky et al., 2020). Donjek Glacier experiences surge episodes approximately every 12 years, with the most recent surges occurring in 1989, 2001, and 2013 (Johnson, 1972a, 1972b; Abe et al., 2016). These surges are confined to a 20 km section near the terminus, where the glacier narrows significantly (Abe et al., 2016).

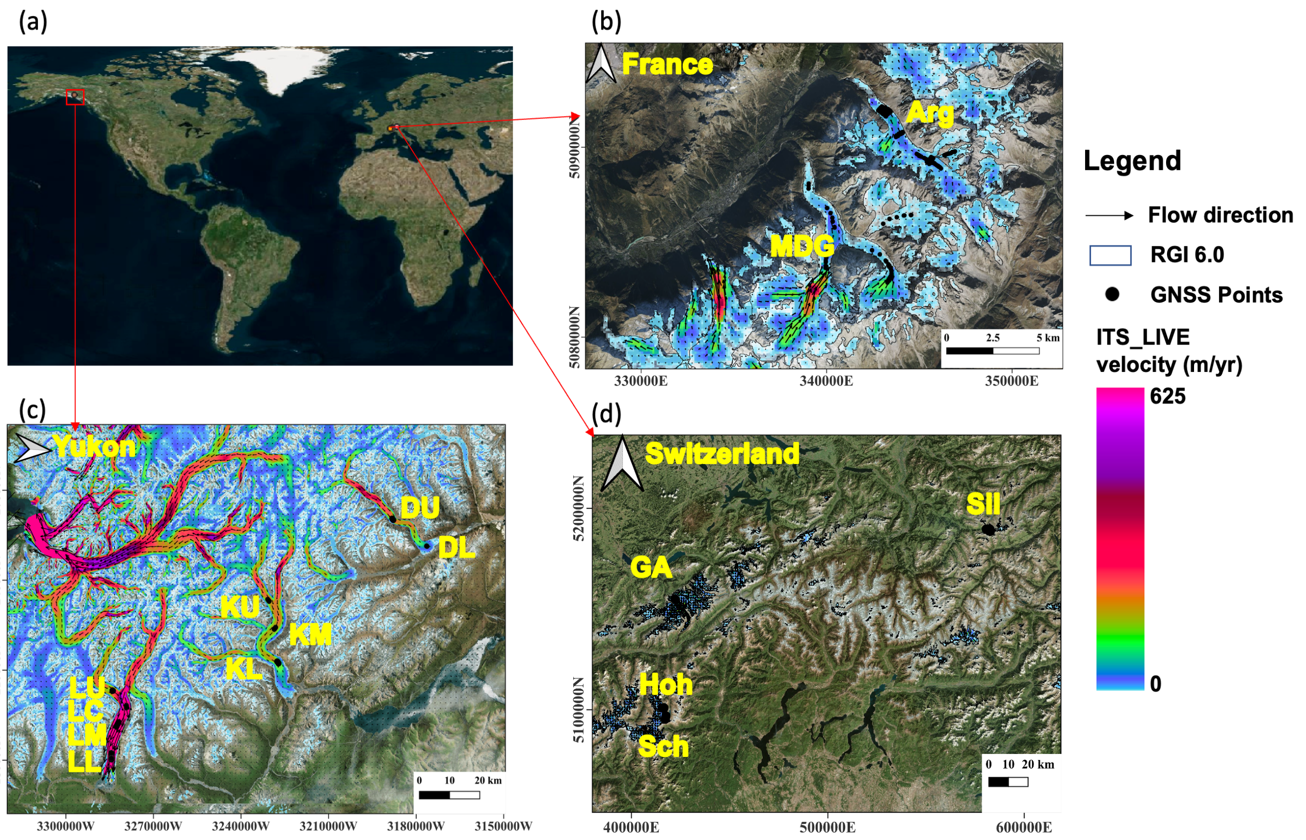

Figure 1: Map of the study areas with GNSS locations. (a) Global location map showing the three study regions; (b) France: Argentière Glacier (Arg) and Mer de Glace (MDG); (c) the Yukon region with GNSS locations: Donjek Upper (DU), Donjek Lower (DL), Kaskawulsh Upper (KU), Kaskawulsh Middle (KM), Kaskawulsh Lower (KL) and Lowell Upper (LU), Lowell Corner (LC), Lowell Middle (LM), Lowell Lower (LL); (d) Switzerland: Grosser Aletschgletscher (GA), Hohlaubgletscher (Hoh), Schwarzberggletscher (Sch) and Silvrettagletscher (Sil). Black outlined polygons indicate RGI 6.0 glacier boundaries. Black arrows indicate glacier flow direction. Black dots mark GNSS measurement points. Each GNSS point, along with its distance to the nearest ice-free surface, is shown in Supplement Figures S1, S2, and S3.

2.2 France

The GNSS stations used in this study are located on two glaciers: Argentière Glacier and Mer de Glace (Fig. 1b). Argentière Glacier, situated in the Mont-Blanc range of the French Alps (45°55’N, 6°57’E), exhibits distinct seasonal variations in its ice flow (Vincent et al., 2022). In 2003, this northwest-facing glacier covered an area of 12.4 km² and stretched roughly 10 km. Its elevation ranges from 3,400 m a.s.l. at the upper accumulation zone down to 1,600 m a.s.l. at the terminus (Rabatel et al., 2018). With the exception of the lowermost tongue situated below the icefall (2,000–2,400 m a.s.l.), the glacier surface is mostly free of rock debris (Vincent et al., 2022).

Mer de Glace (45◦55′ N, 6◦55′ E) spans approximately 12 km in length. The glacier is fed by extensive accumulation basins, specifically the Géant system to the southwest and the Leschaux and Talèfre tributaries from the southeast (Peyaud et al., 2020). The convergence of these tributaries produces prominent medial moraines along the main trunk. Elevations across the system range from high accumulation zones above 3,500 m a.s.l. (rising toward 4,000 m along the surrounding ridgelines) down to a debris-covered lower tongue near 1,500–1,700 m a.s.l. (Peyaud et al., 2020).

2.3 Switzerland

The GNSS stations used in this study are located on four glaciers: Grosser Aletschgletscher, Hohlaubgletscher, Schwarzberggletscher and Silvrettagletscher. The Grosser Aletschgletscher is the largest glacier in the Alps. Its morphology is defined by three large accumulation basins that converge at Konkordiaplatz to form a distinctively curved, extended glacier tongue. In 1999, the Grosser Aletschgletscher measured approximately 22 km in length and covered an area of 83 km² (Bauder et al., 2017).

The Hohlaubgletscher is a temperate mountain glacier (Huss et al., 2017) located in the Pennine Alps, Switzerland, with a surface area of 2.256 km² as of 2004 (GLAMOS). The glacier flows in a northeasterly direction, extending from a headwall at approximately 3,860 m a.s.l. down to a terminus at 2,680 m a.s.l. (GLAMOS).

The Schwarzberggletscher is a narrow valley glacier in the Pennine Alps (canton of Valais, Switzerland). It drains the north–northwest flanks of the Strahlhorn–Rimpfischhorn massif toward the Saas Valley. The glacier comprises a compact high-elevation accumulation basin feeding a confined trunk that descends through a rock-bounded corridor with pronounced lateral moraines and trimlines indicative of recent retreat.

Silvrettagletscher (46.85°N, 10.08°E) is a small temperate mountain glacier currently covering 2.7 km², with an elevation range spanning from 2,470 to 3,070 m a.s.l. Its equilibrium line altitude (ELA) averaged 2,775 m a.s.l. over the 1960–1990 reference period (Lopez-Saez et al., 2024).

Table 1: GNSS point location used for validation of the ITS_LIVE datasets

Glacier Point	Glacier Area (km^2)	Point Aspect (degree)	Nearest Rock (m)	Point Slope (degree)	Point elevation (m)	Point location	GNSS Data Source
Donjek Lower	448	93 (E)	2330	26	1201	ablation	Charrier et al., 2025
Donjek Upper	448	348 (NW)	1278	30	1773	ablation	Charrier et al., 2025
Kaskawulsh Lower	1053	67 (E)	2022	14	1161	ablation	Charrier et al., 2025
Kaskawulsh Middle	1053	103 (SE)	2386	6	1528	ablation	Charrier et al., 2025
Kaskawulsh Upper	1053	84 (E)	1348	10	1702	accumulation	Charrier et al., 2025
Lowell Lower	582	130 (SE)	1905	14	788	ablation	Charrier et al., 2025
Lowell Middle	582	129 (SE)	2191	7	1000	ablation	Charrier et al., 2025
Lowell Corner	582	42 (NE)	1575	14	1120	ablation	Charrier et al., 2025
Lowell Upper	582	344 (NW)	2470	12	1220	accumulation	Charrier et al., 2025
Grosser Aletschgletscher	82	66 (NE)	393	4	3329	accumulation	GLAMOS
Hohlaubgletscher Point 1	2	42 (NE)	252	10	3234	accumulation	GLAMOS
Hohlaubgletscher Point 2	2	80 (E)	162	7	3028	-	GLAMOS
Schwarzberggletscher Point 1	5	24 (NE)	353	13	2772	ablation	GLAMOS
Schwarzberggletscher Point 2	5	24 (NE)	498	8	2844	ablation	GLAMOS
Schwarzberggletscher Point 3	5	347 (N)	893	2	2985	accumulation	GLAMOS
Schwarzberggletscher Point 4	5	1 (N)	886	4	3000	accumulation	GLAMOS
Mer de Glace Point 1 (Géant)	24	355 (N)	283	13	1758	ablation	GLACIOCLIM
Mer de Glace Point 2 (Géant)	24	295 (NW)	266	4	1978	ablation	GLACIOCLIM
Mer de Glace Point 3 (Géant)	24	59 (NE)	313	4	2150	ablation	GLACIOCLIM
Mer de Glace Point 4 (Leschaux)	7	321 (NW)	239	8	2450	ablation	GLACIOCLIM

Mer de Glace Point 5 (Talèfre)	7	222 (SW)	289	21	2693	ablation	GLACIOCLIM
Argentière Glacier Point 1	14	335 (NW)	135	4	2382	ablation	GLACIOCLIM
Argentière Glacier Point 2	14	317 (NW)	144	5	2539	ablation	GLACIOCLIM
Argentière Glacier Point 3	14	286 (W)	389	5	2717	ablation	GLACIOCLIM
Argentière Glacier Point 4	14	221 (SW)	99	26	2977	equilibrium-line	GLACIOCLIM

3 Datasets

3.1 ITS_LIVE Version 2 Ice Velocity Products

The ITS_LIVE v2 glacier velocity dataset offers insights into the time-variable flow of glaciers. This dataset is generated using imagery from the Sentinel-1/2 and Landsat-4/5/7/8/9 satellites, employing the Normalized Cross-Correlation (NCC) offset tracking method (Gardner et al., 2025). Specifically, surface velocities are derived using the core processing algorithm of the ITS_LIVE pipeline, which combines a precise geocoding module "Geogrid" (Lei et al., 2021) with an efficient offset tracking module "autoRIFT" (autonomous Repeat Image Feature Tracking; Gardner et al. 2018). The autoRIFT has been subsequently updated by Lei et al. (2021, 2022), and both open-source modules are freely accessible on GitHub (https://github.com/nasa-jpl/autoRIFT; last accessed: April 2, 2026) and are widely used in glaciology as well as other fields (e.g. earthquake (Banerjee et al., 2025) and landslide studies (Walden et al., 2025)).

The ITS_LIVE v2 products (hereafter referred to as ITS_LIVE) used in this work contain scale distortion, as they are representative of the map projection in which they are provided; the implications of this are detailed in Gardner et al. (2025). The standard output variables for all ITS_LIVE image-pair velocity products include *vx* and *vy* (velocity components along the x and y axes of the provided map projection), velocity magnitude (v), associated errors (*vx_error*, *vy_error*, and *v_error*), as well as the correlation kernel dimensions (*chip_size_height* and *chip_size_width*) (Gardner et al., 2025).

Temporal baseline matching was applied to ensure consistency in comparisons between ITS_LIVE and GNSS velocities across all study regions. For the Yukon region, GNSS observations — available at daily resolution — were integrated over the temporal baseline of each corresponding ITS_LIVE image pair, with time intervals ranging from 5 to 730 days. For the Swiss and French Alps, GNSS data were available only at annual intervals; accordingly, ITS_LIVE velocities were averaged over the same annual periods prior to comparison. In total, this study draws on data from nine glaciers across three regions. For the Yukon region, we used Sentinel-1, Sentinel-2, and Landsat-8 image-pair velocity granules comprising 6,350, 10,163, and 2,668 netCDF files, respectively. For the European Alps (Switzerland and France combined), we used 7,179 Sentinel-1, 31,791 Sentinel-2, and 11,673 Landsat-8 netCDF files. Only intra-annual image pairs were used in the European Alps, with time intervals below 365 days.

The ITS_LIVE annual composite dataset provides gridded, year-by-year maps of glacier and ice-sheet surface velocity. It aggregates millions of image-pair velocities into robust annual composites, delivering consistent *vx*/*vy* components, velocity magnitude, and uncertainties for each grid cell (Gardner et al., 2025). To ensure that the annual mean velocity is not biased by the timing of image acquisitions over the course of the year, this dataset applies a mathematical best-fit procedure that accounts for typical seasonal fluctuations in total displacement. An initial fit is first performed using all available observations; outliers are then identified through a median absolute deviation filter and removed, after which the fit is recomputed without them (see Gardner et al., 2025, for details).

3.2 GNSS data

Dense GNSS time series were acquired at Kaskawulsh Glacier (2012–2022), Lowell Glacier (2017–2022), and Donjek Glacier (2018–2022) in the Yukon, Canada. Continuous GNSS measurements were conducted on glaciers between 2013 and 2022, using up to six dual-frequency receivers deployed across glaciers (Waechter et al., 2015; Van Wychen et al., 2023). Two generations of receivers were deployed during the study period: up to and including 2016, Trimble R7 instruments were installed on stakes drilled directly into the glacier ice, while from 2017 onwards, these were progressively replaced by Trimble NetR9 receivers — each connected to a Zephyr Geodetic antenna and mounted approximately 1.5 m above the glacier surface on tripods resting on the ice surface (i.e., floating with the ice rather than anchored into it). Raw GNSS observations were recorded at a 15-second sampling interval, with daily logging windows of 2–3 hours during winter and continuous 24-hour acquisition throughout the summer season (typically May to August). Daily records shorter than 1.5 hours — which occasionally occurred in winter due to insufficient battery supply — were discarded prior to further analysis. All raw observations were post-processed using the Precise Point Positioning (PPP) web service provided by Natural Resources Canada (NRCan; https://webapp.geod.nrcan.gc.ca/geod/tools-outils/ppp.php), yielding typical positioning uncertainties of 1–2 cm horizontally and approximately 5 cm vertically. The dataset used here was pre-processed by Charrier et al. (2025), who removed outliers using a Local Outlier Factor (LOF) algorithm applied to the position gradients. LOF quantifies the local density deviation of each point relative to its temporal neighbours in the time series, flagging points with anomalously low local density as outliers (Charrier et al., 2025). In their tests, this method detected abrupt changes in position gradients more reliably than a running median absolute deviation (MAD) filter (Breuniget al., 2000). A data validity threshold of 80% was applied, following the methodology described in Waechter et al. (2015) and Charrier et al. (2025).

In Switzerland, the GNSS data provided by the Swiss Glacier Monitoring Network (GLAMOS) are freely accessible at https://doi.glamos.ch/data/flowvelocity/flowvelocity_2022_r2022.html.These measurements are derived from ablation stakes whose positions are surveyed with a mobile GNSS receiver approximately once per year. Surveyed stakes on Grosser Aletschgletscher, Schwarzberggletscher, Hohlaubgletscher, and Silvrettagletscher generally span the period 2012–2021. It should be noted that the GNSS data for Grosser Aletschgletscher were collected in the accumulation zone (Fig. S1 (d)).

In France, we used in situ differential GNSS measurements from the glacier observatory GLACIOCLIM, which provides multidecadal observations for key glaciers in the French Alps, including Argentière Glacier and the Mer de Glace, to validate our glacier surface velocity measurements (https://glacioclim.osug.fr/Donnees-des-Alpes). Annual topographic surveys of the ablation stakes (surface flow velocities) and of the cross-sectional profiles (thickness variations) are carried out using conventional surveying methods or differential GPS geodetic receivers (one receiver on a known fixed point and a mobile receiver on the points to be determined), once a year, in September. Surface flow velocities are expressed in metres per year and are measured with an accuracy of about 5 cm (https://glacioclim.osug.fr/Mesures-glaciologiques). For the Mer de Glace (MDG), the temporal coverage varies by tributary: Leschaux: 2007–2019, Tacul tongue:1995–2019, and Talèfre: 2007–2018. For Argentière Glacier, the temporal coverage is Tour Noir: 2005–2018 and for profiles 2, 4, 5, and 7: 2015–2019.

4 Method

In this section we describe the methodology for comparing ITS_LIVE image-pair velocities with the GNSS dataset. We developed separate GNSS processing chains for the dense daily time series data over the Yukon region, and for the annual interval data over France and Switzerland, respectively (Zhang et al., 2024). Before comparison, a coordinate transformation is required to match both the location and the velocity component in the GNSS projected coordinate systems with that in the ITS_LIVE map-projected coordinate system.

4.1 Coordinate transformation

The GNSS datasets are first reprojected to the ITS_LIVE map coordinate system. As illustrated in Fig. 2, the first step is to convert the start location (i_s, j_s) of each GNSS point from its native projected coordinate system to the ITS_LIVE coordinate system. The GNSS time interval is Δt. Next, we compute the displacement components dx and dy — representing the distances between the start and end points of the GNSS trajectory along the x and y axes, respectively — within the GNSS projected coordinate system, as given by Equations (1) and (2):

$$dx = \Delta t * vx \quad (1)$$

$$dy = \Delta t * vy \quad (2)$$

These displacement components are derived from the corresponding GNSS velocity components vx and vy. The end location is then calculated as:

$$i_e = i_s + dx;\ j_e = j_s + dy \quad (3)$$

we convert i_e and j_e from the GNSS projected coordinate system to the ITS_LIVE map coordinate system. Once both the start and end positions are reprojected into the ITS_LIVE map coordinate system, updated displacement components dx' and dy' are calculated. These are then used to derive the reprojected GNSS velocity components vx' and vy' , as well as the total velocity magnitude v', all referenced to the ITS_LIVE map projection.

This reprojection procedure ensures that GNSS velocities are expressed in the same map projection as the ITS_LIVE velocity fields, so that the vx and vy components are aligned with the same Easting and Northing directions in both datasets for most UTM zones. For the Swiss glaciers, points were reprojected from the Swiss national coordinate system CH1903/LV03

(EPSG:21781) to WGS 84 / UTM zone 32N (EPSG:32632). For the French glaciers, points were reprojected from NTF (Paris) / Lambert zone II (EPSG:7411) to WGS 84 / UTM zone 32N (EPSG:32632). However, for the Yukon region, each GNSS observation point was reprojected from WGS 84 / UTM zone 7N (EPSG:32607) to the Polar Stereographic North projection (EPSG:3413). In the Polar Stereographic North projection (EPSG:3413), the Y-axis is oriented toward the central meridian (45°W), and the X-axis points 90° counterclockwise from it. Since the Yukon region is located approximately 90° west of this central meridian (~135°W), the projected axes are rotated ~90° relative to the local geographic directions. Therefore, the X-axis corresponds approximately to the Northing direction and the Y-axis corresponds approximately to the Easting direction in this region — the opposite of the standard UTM convention. This axis rotation was explicitly accounted for by reassigning the projected axis components accordingly using the above-mentioned methods when comparing *vx* and *vy* velocity components between the GNSS and ITS_LIVE datasets.

Table 2: GNSS data used for validation of the ITS_LIVE datasets.

Name	Yukon	Switzerland	France
GNSS data	Dense time series (daily)	Annual	Annual
Number of Glaciers	3	4	2
Number of GNSS sites	9	25	68
GNSS time period	2017-2022	2013-2021	2012-2020
ITS_LIVE Sensors	Sentinel-1, Sentinel-2, Landsat-8	Sentinel-1, Sentinel-2, Landsat-8	Sentinel-1, Sentinel-2, Landsat-8

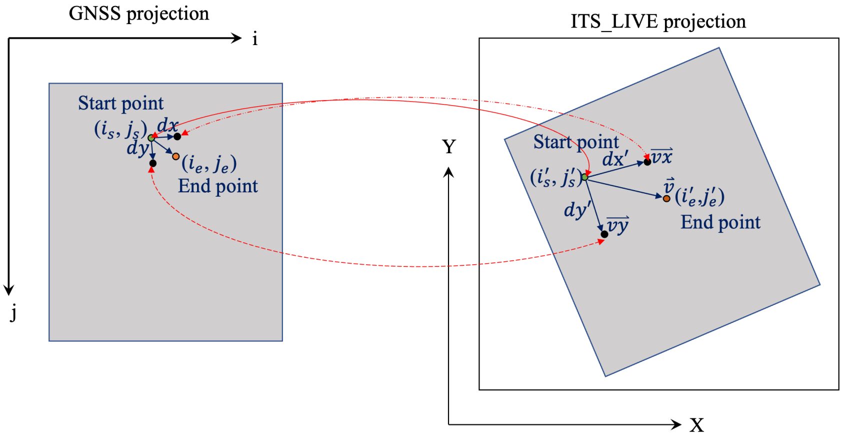

Figure 2: The GNSS coordinates (i, j) of the start and end points are projected onto the ITS_LIVE coordinate system (X, Y), to be directly comparable to the ITS_LIVE velocities. Given a small increment dx in the i-direction (or dy in the j-direction), the induced displacement vector in (X, Y) is derived through coordinate transformation. Lastly, we calculate the GNSS velocity components expressed in the ITS_LIVE projection: $\overrightarrow{vx}$, $\overrightarrow{vy}$, and $\vec{v}$ respectively.

4.2 Validation processing chain using dense time series of GNSS data

For the dense time series of GNSS data in the Yukon region, we implemented a two-step approach to remove outliers from the ITS_LIVE image-pair time series dataset (Fig. 3): error thresholding and spatial filtering (Rabatel et al., 2023; Lei et al., 2022). The time interval ranges between 5 and 730 days. Below are the two steps:

a. Error thresholding: Eliminate the ITS_LIVE point if any of the uncertainty in velocity components (*vx_error*, *vy_error*) or magnitude (*v_error*) associated with the ITS_LIVE product is larger than 40 m/yr. According to the *v_error* shown in Lei et al., (2022), the uncertainty of ITS_LIVE is 50-70 m/yr for fast-moving glaciers, such as Jakobshavn Isbræ glacier (Lei et al., 2022). ITS_LIVE feature-tracking errors are quantified over stable terrain. For Sentinel-1A/B, the optimal 6-day pair yields X- and Y-direction errors of 12 m/yr and 39 m/yr, respectively, whereas Landsat-8 with a 16-day separation produces corresponding errors of 22 m/yr and 31 m/yr (Lei et al., 2021). After several thresholding trials, we decided on a threshold of 40 m/yr for small-scale mountain glaciers (which exhibit lower velocities than larger-scale glaciers). This threshold removes most of the inaccurate ITS_LIVE product pairs relative to the small-scale glaciers' velocities. The 40 m/yr threshold is well-grounded in three complementary lines of evidence: (1) it is conservatively below the known large-glacier error range of 50–70 m/yr (Lei et al., 2022); (2) it aligns closely with the worst-case stable-surface error of Sentinel-1 (~39 m/yr (Lei et al., 2021)); and (3) it was empirically confirmed through iterative testing to optimally balance data quality and retention of sufficient samples for small-scale mountain glaciers. Together, these factors provide a physically and statistically coherent rationale for the chosen threshold.

b. Spatial filtering: For each measurement U_0, the median U_m of the 24 surrounding value in a 5 × 5 neighborhood (U_1, $U_2, \ldots, U_{25}$) is calculated (excluding U_0), and for each value in the neighborhood, a residual $Ri = |Ui - Um|$ is calculated. The median R_m of the set ($R_1, R_2, \ldots, R_{24}$) is subsequently computed and applied to normalize the residual of U_0 such that:

$$R0 = |U0 - Um|/(Rm + \varepsilon) \qquad (4)$$

here, ε is defined as a minimum normalization value that captures the effect of cross-correlation noise. We adopt $\varepsilon = 0.1$ pixels, as proposed by Westerweel and Scarano (2005), and remove the measurement U_0 if R_0 exceeds a threshold of 5 in either the *vx* or *vy* direction (Solgaard et al., 2021).

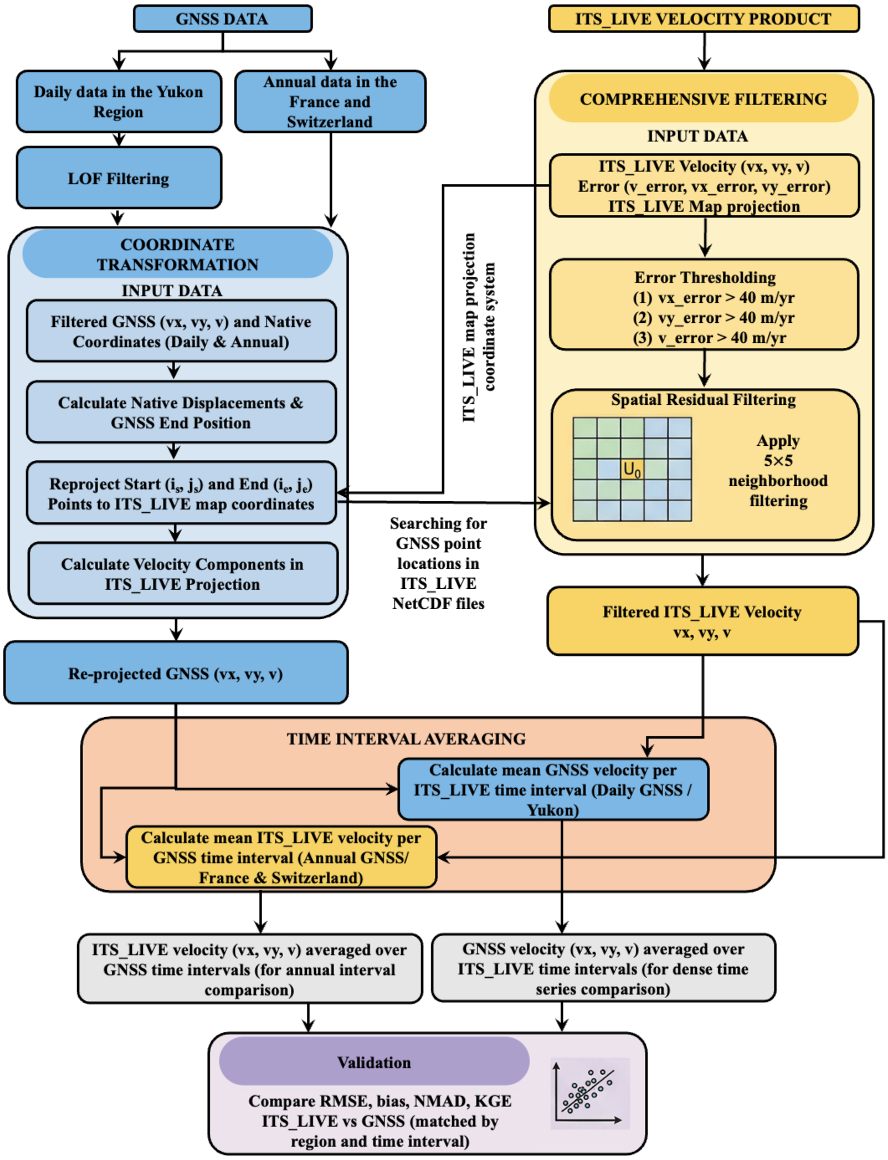

Figure 3: Flow chart of the data processing chain validating ITS_LIVE image-pair velocity against a dense time series of GNSS data

4.3 Validation processing chain using annual GNSS data

For the annual GNSS dataset, we did not apply the filters described above. In order to match the GNSS annual velocities at specific locations, the corresponding ITS_LIVE velocities were extracted for the same sites and the same annual time intervals. Here, we demonstrate two types of annual data results. The first uses all available ITS_LIVE image pairs within the annual intervals of GNSS measurements, where all ITS_LIVE values within each year are averaged and then further compared with the annual GNSS velocities.

The second approach is to directly use the ITS_LIVE-produced annual composite dataset. The annual composite maps are generated by computing the error-weighted least-squares fit to all image-pair velocity fields with center dates falling within the same calendar year. More details can be found in Gardner et al. (2025).

4.4 Accuracy assessment

To assess the accuracy of the ITS_LIVE velocities, we compared the ITS_LIVE data with the GNSS data over the same time period, illustrated as density scatterplots of *v* (*vx* and *vy* are used instead for Sentinel-1 SAR to differentiate range/azimuth directions). The error metrics used in this work include root mean square error (RMSE), mean bias, and normalized median absolute deviation (NMAD) (Rousseeuw and Croux, 1993)

$$NMAD = 1.4826 \times median(|X_i - \tilde{X}|) \tag{5}$$

where $\tilde{X}$ is the median of the sample $X_1, X_2, \ldots, X_n$. NMAD is a robust alternative to the standard deviation. It is less sensitive to outliers than the classical standard deviation. We also compute the Kling–Gupta Efficiency (KGE), a goodness-of-fit metric first proposed by Gupta et al. (2009) for calibrating hydrological models, which evaluates the reproduction of peak flows and seasonal variability. Owing to its ability to partition error into bias, variability, and correlation terms, the KGE has become increasingly popular in glaciological research. It is defined as:

$$KGE = 1 - \sqrt{(r-1)^2 + (\alpha-1)^2 + (\beta-1)^2} \tag{6}$$

where r is the Pearson's correlation coefficient, $\alpha = \frac{\sigma_e}{\sigma_o}$ with σ_e and σ_o being the standard deviation of the estimated and observed time-series, respectively, and $\beta = \frac{\mu_e}{\mu_o}$ with μ_e and μ_o being the means of the estimated and observed time-series, respectively. Here, α reflects the relative variability ratio of the estimation, whereas β serves as the bias term. Achieving a KGE of 1 signifies that the estimated and observed time-series match perfectly. (Gupta et al., 2009).

5 Results and analysis

In this section, the ITS_LIVE datasets derived from the three primary sensors (Sentinel-1, Sentinel-2 and Landsat-8) are used for comparison with both dense time series and annual GNSS data. Section 5.1 presents the dense time-series comparison results for the Yukon region, followed by the annual image-pair and annual composite comparison results for the Swiss and French Alps in Section 5.2.

https://doi.org/10.5194/egusphere-2026-2541
Preprint. Discussion started: 12 June 2026

5.1 Dense time series comparison with GNSS in Yukon, Canada

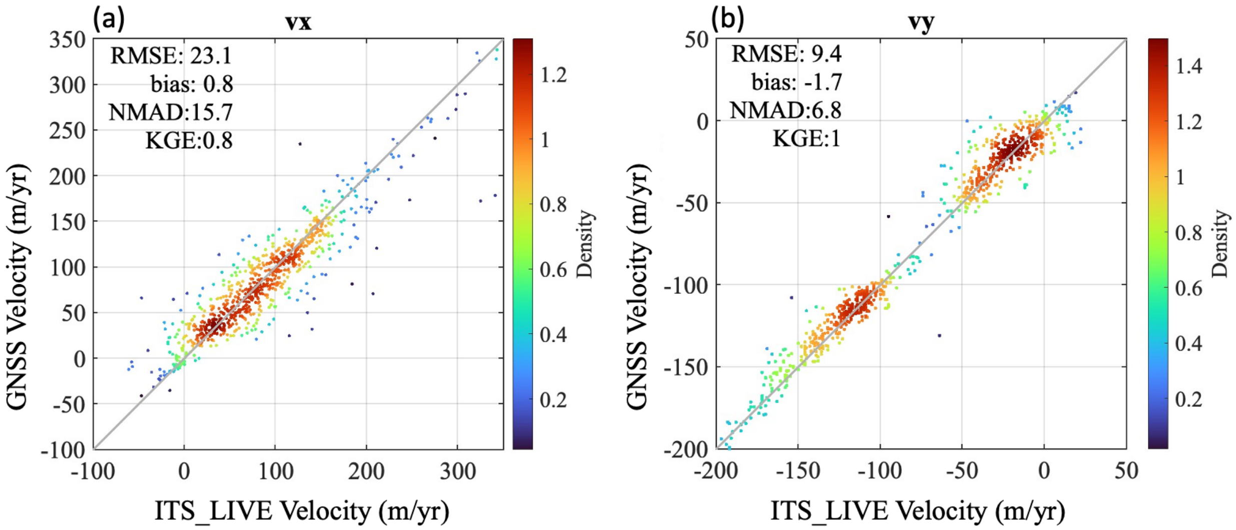

Figure 4: Density scatterplot comparison of ice motion velocity (*vx* and *vy*) between dense time series GNSS data and ITS_LIVE Sentinel-1 image-pair products for all GNSS points in the Yukon region. A negative bias indicates that ITS_LIVE underestimates the velocity relative to the GNSS measurements.

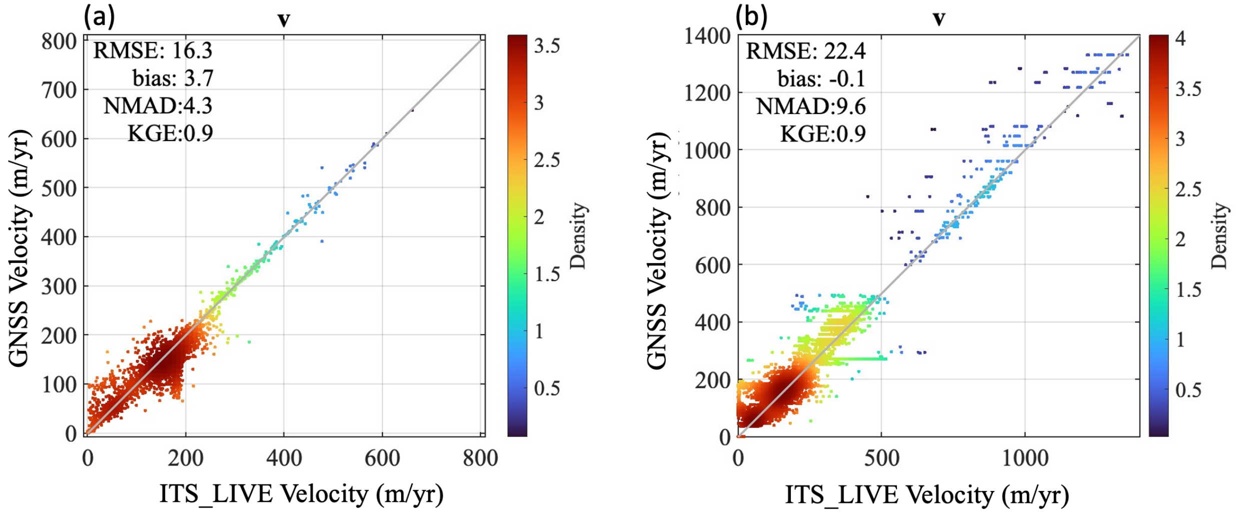

Figure 5: Density scatterplot comparison of ice motion velocity magnitude (v) between dense time series GNSS data and ITS_LIVE image-pair products for all GNSS points in the Yukon region. Landsat-8 (left) and Sentinel-2 (right). A negative bias indicates that ITS_LIVE underestimates the velocity relative to the GNSS measurements.

The Yukon study sites include the Donjek, Kaskawulsh, and Lowell glaciers. Using the methodology described in Section 4.2 (Fig. 3), we present density scatterplots for all three glacier sites in the Yukon region. In Fig. 4, both components of the ITS_LIVE Sentinel-1 velocity measurements (*vx* and *vy*) are compared with the corresponding GNSS-derived velocity components. The RMSE for the *vy* component (9.4 m/yr; Fig. 4b) is lower than that for the *vx* component (23.1 m/yr; Fig. 4a). This is because the *vy* component roughly corresponds to the Sentinel-1 range direction, while the *vx* component corresponds to the azimuth direction, and Sentinel-1 achieves higher measurement precision with a factor of 3 in the range direction than in the azimuth direction (Mouginot et al., 2017; Joughin et al., 2018; Lei et al., 2022). The Donjek, Kaskawulsh, and Lowell glaciers generally flow from west to east. As a result, the majority of their motion is captured in the *y* direction. Fig. 4b shows a high density of velocity values between –150 and -100 m/yr, which corresponds to the typical flow velocities of the lower reaches of the Kaskawulsh glacier. A secondary density peak between –50 and 0 m/yr represents the normal glacier flow of the slower-moving sections. The scatterplots of ITS_LIVE Landsat-8 and Sentinel-2 velocities (*v*) compare well with GNSS velocities (Fig. 5), with KGE 0.9. Sentinel-2 exhibits a lower bias (−0.1 m/yr) compared to Landsat-8 (3.7 m/yr). However, these bias values should be interpreted with caution, as their magnitudes are small relative to the overall measurement uncertainty reflected by the RMSE values of both Landsat-8 (16.3 m/yr) and Sentinel-2 (22.4 m/yr). When the RMSE is much larger than the bias, it becomes statistically difficult to determine whether the detected bias reflects a true systematic offset or simply random error fluctuation. The highest density range (0–200 m/yr) corresponds to the typical mountain glacier flow velocities. Both Landsat-8 and Sentinel-2 successfully captured the glacier surge event that occurred between May and July 2022, as indicated by velocities exceeding 500 m/yr.

Sentinel-2 likely provides more short-interval image pairs than Landsat-8, owing to its 5-day repeat cycle from its two-satellite constellation. In addition, Sentinel-2 offers higher spatial resolution (10 m) compared to the Landsat-8 panchromatic band (15 m), which may further improve the accuracy of feature tracking at shorter temporal baselines. Fig. 5 shows higher velocities retrieved by Sentinel-2 compared to Landsat-8. The results of this analysis reveal a nuanced trade-off between the two sensors. While the Landsat-8 data exhibits a lower RMSE (16.3 m/yr) and NMAD (4.3 m/yr), its performance is compromised by a substantial bias of 3.7 m/yr. Conversely, the Sentinel-2 data, with an RMSE of 22.4 m/yr and an NMAD of 9.6 m/yr, demonstrates negligible bias (-0.1 m/yr).

5.2 Comparison with annual GNSS data

First, we compare the simple annual averages of ITS_LIVE image-pair products with annual GNSS measurements (Fig. 6). The French glacier data points are more scattered than the Swiss ones (RMSE of 40.9–55.2 m/yr; bias of −28.5–40 m/yr). In France, ITS_LIVE Sentinel-1 velocities are concentrated around 60–100 m/yr, whereas GNSS velocities are around 40–60 m/yr. The higher ITS_LIVE Sentinel-1 velocities relative to GNSS reflect a positive bias of up to 40 m/yr, indicating substantial overestimation and high scatter. The bias may be due to the coarse resolution of Sentinel-1 leading to a larger pixel-level displacements (see section 6.1). Sentinel-1 has a larger RMSE (55.2 m/yr) than Sentinel-2 (44 m/yr) and Landsat-8 (40.9 m/yr) for the French sites. Both Sentinel-2 and Landsat-8 show poor agreement, but Landsat-8 has slightly lower scatter than Sentinel-2 (NMAD of 29.3 m/yr for Landsat-8 and 43.6 m/yr for Sentinel-2). Over the French sites, ITS_LIVE Sentinel-2 and Landsat-8 underestimate glacier velocity, retrieving values of roughly 0–40 m/yr compared to GNSS velocities of 40–60 m/yr (bias of −28.5 m/yr and −22.5 m/yr, respectively). The three negative KGE values reveal a poor correlation between ITS_LIVE and GNSS measurements. When considering glacier width (Figure S2: (a) Mer de Glace; (b) Argentière Glacier), some points are located near bedrock, about 60–140 m from the glacier margin. With a chip size of 240 m, ITS_LIVE measurements are very likely to include side rock adjacent to the glacier, leading to an underestimation of glacier velocity (see section 6.2). Overall, the Swiss data show much better agreement between the ITS_LIVE and GNSS measurements (RMSE of 11.5–19.4 m/yr; bias of 5.5–15.3 m/yr). Over the Swiss sites, ITS_LIVE Sentinel-2 and Landsat-8 overestimate glacier velocity, retrieving values of 10–25 m/yr (bias of 10.0 m/yr and 15.3 m/yr, respectively) for small-scale glaciers whose GNSS-measured velocities are 0–10 m/yr. Although the Swiss RMSE values are small (11.5–19.4 m/yr), the KGE remains negative (down to −1.5 for Landsat-8): the narrow dynamic range of the Swiss velocities suppresses the absolute error (see section 6.3). This demonstrates that a low RMSE alone does not indicate a reliable velocity retrieval, and that the lack of agreement is revealed by the KGE.

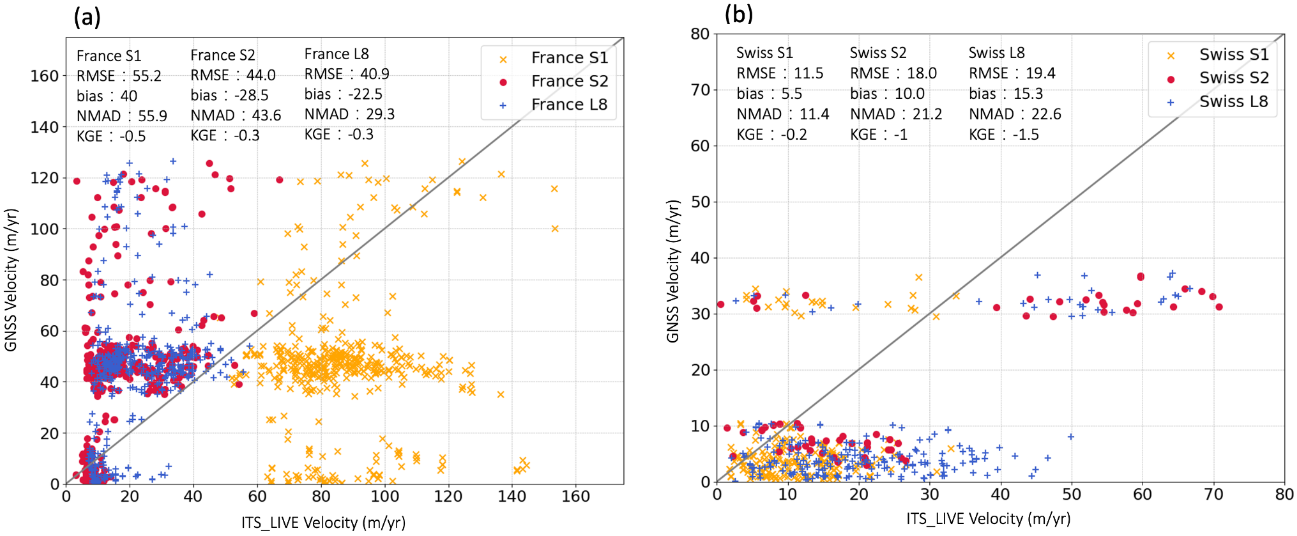

Figure 6: Scatterplot comparison of ice motion velocity magnitude (v) between annual GNSS data and simple annual averages of ITS_LIVE image-pair products for all GNSS points in the France (a) and Switzerland (b) study sites. Data from all three sensors—Sentinel-1, Sentinel-2, and Landsat-8 are included in the comparison. A negative bias indicates that ITS_LIVE underestimates the velocity relative to the GNSS measurements.

Next, we compare the ITS_LIVE annual composite product with annual GNSS measurements, as shown in Fig. 7. The agreement between ITS_LIVE annual composites and GNSS data is better over the Swiss sites (RMSE of 5.7 m/yr, NMAD of 2.7 m/yr, KGE of 0.7) compared to the French sites (RMSE of 41.9 m/yr, NMAD of 46.7 m/yr, KGE of −0.1). These points occur on smaller glaciers, such as those at Hohlaubgletscher (Fig. S1(c), Schwarzberggletscher and Silvrettagletscher. Many France points are concentrated in the region where ITS_LIVE < 25 m/yr, while the corresponding GNSS velocities range from approximately 25 to 70 m/yr or even higher, indicating relatively large errors in the low-velocity range. These points are mainly located at Mer de Glace Points 3 and 4 (Supplementary Fig. S2a). Specifically, they are located on the Tacul and Leschaux glaciers, which are tributary glaciers of the Mer de Glace system; the low coherence likely due to spatial heterogeneity and the proximity of these points to stable terrain. A more detailed discussion is provided in Section 6.2. Comparing Fig. 7 with Fig.

6, it can be observed that ITS_LIVE annual composite product has lower bias (-1.2 m/yr in Switzerland and -28.9 m/yr in France) than simple annual averages of ITS_LIVE image-pair products (bias 5.5-15.3 m/yr in Switzerland and -28.5-40 m/yr in France), suggesting that the error-weighted least-squares fitting approach used in the annual composite product partially mitigates systematic biases present in the averages of individual image pairs.

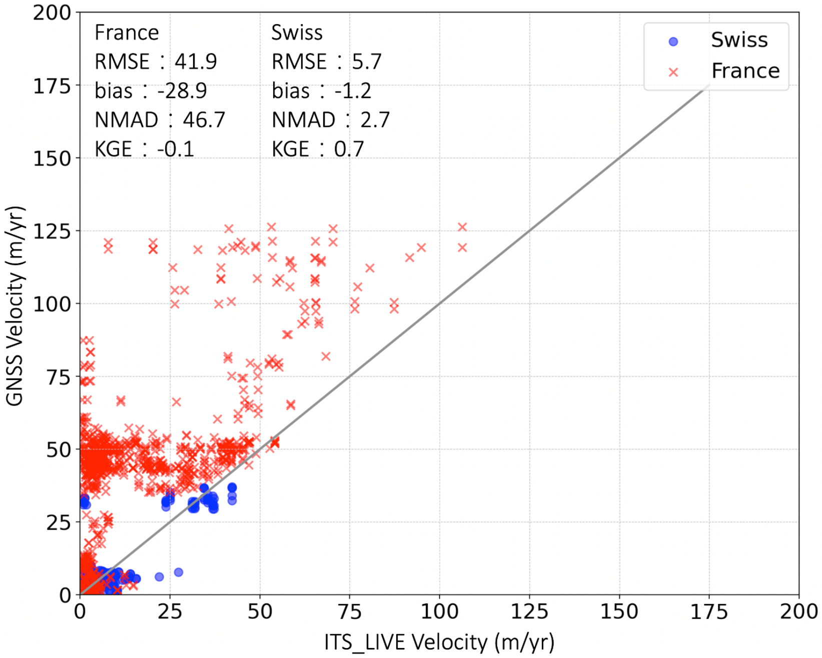

Figure 7: Scatterplot comparison of ice motion velocity (v) between annual GNSS data and ITS_LIVE annual composite products, for all measurement points in France and Switzerland.

Since Sentinel-1 is a SAR sensor with inherently anisotropic measurement characteristics — differing precision in the range and azimuth directions — we decompose the velocity into *vx* and *vy* components to better analyze the directional sources of error. In Fig. 8, both *vx* and *vy* components of the Swiss data points are well aligned with the 1:1 line (*vx*: RMSE 5.1 m/yr, bias −0.6 m/yr; vy: RMSE 13.4 m/yr, bias 2.4 m/yr), which is consistent with the results shown in Figs. 6 and 7. In contrast, the French data points are considerably more scattered than the Swiss counterparts, with NMAD values of 29.3 m/yr (*vx*) and 38.7 m/yr (*vy*) compared to 4.9 m/yr (*vx*) and 13.8 m/yr (*vy*) for the Swiss sites, respectively. The France Sentinel-1 *vy* component is the main source of disagreement, showing large scatter, a high RMSE of 46.3 m/yr, and a strong negative bias of −24.9 m/yr. Many GNSS velocities reach 20–120 m/yr, whereas the corresponding ITS_LIVE velocities are much lower, commonly ranging from about −25 to 50 m/yr. This indicates an underestimation or mismatch in the ITS_LIVE *vy* component. Over the French sites, ITS_LIVE *vx* consistently overestimates glacier velocity (bias of 13.2 m/yr, RMSE of 23.2 m/yr). The reason is discussed in detail in relation to glacier geometry and the location of GNSS points near stable terrain (see section 6.1 and 6.2).

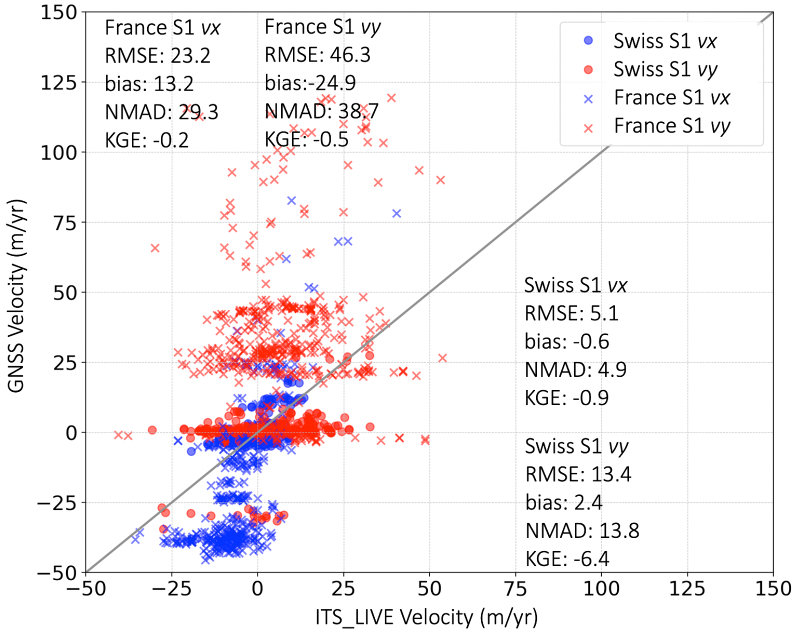

Figure 8: Scatterplot comparison of ice motion velocity (*vx* and *vy*) between annual GNSS data and simple annual averages of ITS_LIVE Sentinel-1 image-pair products, for all measurement points in France and Switzerland.

6 Discussion

6.1 Comparison between satellites

The following section presents a discussion of velocity retrievals across the different sensors employed in this study. The accuracy of ITS_LIVE velocity retrievals differs systematically between the east-west (vx) and north-south (vy) components. Sentinel-1 is inherently more sensitive to displacements in the across-track direction. In contrast, vy estimates are less precise due to the coarser azimuth resolution (15.6 m) relative to the ground-range resolution (3.7 m), a limitation that is reflected in the error metrics shown in Fig. 4 and Fig. 8. This anisotropy stems from the use of Interferometric Wide Swath (IW) SAR mode in ITS_LIVE Sentinel-1 processing, which introduces an asymmetry between range and azimuth precision that disproportionately affects the north-south velocity component. The lower accuracy of the azimuth velocity component is further amplified by atmospheric effects. Lei et al. (2022) report that variations in the ionospheric total electron content affect Sentinel-1 C-band acquisitions, producing significant velocity errors specifically in the azimuth direction. In agreement with these ionospheric effects, Andersen et al. (2020) compared Sentinel-1 offset-tracking results with in situ measurements and found a bias of 2.8 m/yr in range but considerably larger biases of −5.2 to −9.5 m/yr in azimuth, confirming the systematically lower accuracy of the azimuth component. These reported azimuth-range discrepancies are consistent with our own results: in France, the Sentinel-1 bias is 13.2 m/yr in *vx* but −24.9 m/yr in *vy*, while in Switzerland it is −0.6 m/yr in *vx* and 2.4 m/yr in *vy*. In both regions, the *vx* (range) bias is consistently smaller than the *vy* (azimuth) bias. A related but distinct advantage of

SAR-based retrievals is evident in the Grosser Aletschgletscher accumulation zone (Fig. S1(d)), where Sentinel-1 consistently outperforms both Landsat-8 and Sentinel-2. This performance is likely due to the penetration of SAR signals through snow and firn (Kelly et al., 2023); optical sensors additionally struggle to track surface features in this zone owing to the spectrally homogeneous appearance of fresh snow. This case illustrates the complementary nature of SAR and optical velocity products, and underscores that sensor selection should be guided by the specific glaciological zone under investigation.

Differences in optical sensor characteristics further explain the variability in velocity accuracy. The higher spatial resolution of Sentinel-2 (10 m) compared to the Landsat-8 panchromatic band (15 m) provides a greater number of pixels within each 240 m chip, allowing the NCC algorithm to resolve finer surface features and achieve a higher Signal-to-Noise Ratio (SNR) in the correlation output. This translates to a lower velocity error (*v_error*) over stable surfaces and improved discrimination between true ice displacement and noise. A further advantage of Sentinel-2 lies in its higher temporal sampling. The combined Sentinel-2A/2B constellation offers a 5-day repeat cycle, substantially shorter than the 16-day cycle of Landsat-8. This denser temporal coverage yields a richer velocity time series and improves the ability to resolve short-term and rapid glacier dynamics. Yang et al. (2024) quantified this benefit, reporting that Sentinel-2 attains a 26 % lower daily-velocity RMSE than Landsat-8/9, with reported RMSE values of 22–77 m/yr for Sentinel-2 and 58–106 m/yr for Landsat-8/9. Our results, however, reveal a more complex picture in which the relative performance of the two sensors varies by region. In the Yukon, Sentinel-2 yielded an RMSE of 22.4 m/yr compared with 16.3 m/yr for Landsat-8, indicating that the denser Sentinel-2 sampling does not necessarily translate into lower errors where surface conditions are characterized by rapid glacier dynamics. In the French Alps, the two sensors performed comparably (44.0 m/yr for Sentinel-2 versus 40.9 m/yr for Landsat-8), as did those in Switzerland (18.0 m/yr versus 19.4 m/yr, respectively). These results suggest that, although Sentinel-2 provides clear advantages in temporal resolution, its accuracy relative to Landsat-8 is strongly modulated by local factors such as surface texture, glacier geometry, and topographic shadowing, rather than temporal sampling alone.

Despite these advantages in spatial resolution and temporal sampling, Sentinel-2 does not universally outperform other sensors. In the velocity range of 600–1000 m/yr, ITS_LIVE underestimation may be linked to chip overlap with adjacent rock surfaces, while larger uncertainties at high velocities are likely associated with glacier surge events, which can cause abrupt surface changes between acquisition dates (Liu et al., 2024). Millan et al. (2019) found that Sentinel-2 is roughly twice as precise as Landsat 7/8. However, even with Sentinel-2, retrieving reliable velocities over the smallest glaciers (<250 m wide) remains difficult. This is consistent with our study, which shows that the accuracy of glacier velocity estimates depends on the distance from the measurement point to stable terrain.

Sentinel-2 is better suited for resolving fine-scale surface displacements on temperate glacier tongues, while Sentinel-1 offers advantages in snow-covered accumulation zones where optical tracking fails. However, Sentinel-1 is prone to temporal decorrelation at time intervals exceeding 60 days, which limits its effectiveness over longer baselines. The choice of sensor should therefore consider both the spatial characteristics of the target glacier and the surface conditions expected during the observation period.

6.2 Comparison between study area and glaciers

The larger underestimation observed in annual French datasets likely reflects the heterogeneity of French glaciers compared to the Swiss glaciers. Two compounding factors can explain this pattern: the proximity of measurement points to ice-free terrain (Kaab et al., 2016), and the use of a large chip size to accommodate spatially complex glacier geometries.

The nearest rock distance is one of the most critical factors affecting ITS_LIVE accuracy over small mountain glaciers, given the 240 m chip size used in NCC processing. When the distance to the nearest exposed rock is smaller than or comparable to the chip radius (~120 m), the correlation window risks incorporating surrounding ice-free terrain, which dilutes the glacier velocity signal and systematically biases estimates toward lower velocities. This effect is further compounded by the non-uniform velocity field within the chip: glacier velocity naturally decreases toward the margins, so averaging over a 240 m window produces a systematically lower estimate than a localised measurement at the glacier centerline. Together, these two effects — lateral contamination by stable terrain and velocity gradients within the chip — explain the underestimation of ITS_LIVE velocities in France visible in Figs. 6 and 7 (see also Fig. S2 for glacier width context). For the French Alps, Millan et al. (2019) reported comparable weighted standard deviations of 12.4 m/yr and 12.8 m/yr in the accumulation and ablation zones, respectively.

As shown in Table 1, the three study regions differ substantially in nearest-rock distance. The French glacier points (Mer de Glace and Argentière) have the smallest distances, ranging from 99 to 389 m, meaning the 240 m chip frequently overlaps with bedrock or lateral moraines Fig. S2. Swiss glacier points span an intermediate distance-to-margin range (162–893 m). Among these, the most margin-proximal points — Hohlaubgletscher Point 2 (162 m) and Point 1 (252 m) — exhibit the greatest susceptibility to chip contamination within the Swiss dataset (Fig. S1(c)). Schwarzberggletscher (Fig. S1(a)) and Silvrettagletscher (Fig. S1(b)) are characterized by distance-to-margin ranges of 353–892 m and 112–299 m, respectively. In contrast, the Yukon glacier points (Fig. S3) have considerably larger nearest-rock distances (1,278–2,470 m), placing them well within the glacier interior and allowing the chip to sample purely glacial ice, which is consistent with the lower errors observed in that region. Our finding that velocity accuracy depends on the distance to stable terrain is further corroborated by Millan et al. (2019). Using a 50 m Sentinel-2 velocity product, they observed substantial disagreement between GPS and satellite-derived velocities over glaciers narrower than 250 m, with GPS values spanning 0–40 m/yr but Sentinel-2 values reaching only 0–20 m/yr. This systematic underestimation over narrow glaciers mirrors the bias we identify in ITS_LIVE retrievals, where the 240 m correlation chip frequently overlaps adjacent ice-free terrain.

Beyond proximity to rock, surface heterogeneity also plays an important role, as French glacier surfaces are considerably more heterogeneous compared to Swiss ones. The Mer de Glace, for example, is formed by the confluence of the Leschaux and Géant glaciers, after which it flows northwestward as it descends into the Chamonix Valley. Its trajectory is constrained by a deep, U-shaped valley, and its flow dynamics are strongly shaped by the merging of these tributary glaciers and the surrounding topography. When ITS_LIVE computes the north–south velocity component (*vy*), the glacier's sharp bends may cause 240 m search chips to either overlap with stable bedrock on the valley sides or lock onto medial moraines that appear stationary to the correlation algorithm. Both effects introduce errors into the NCC processing and result in an underestimation of the true *vy*. In summary, while a chip size of 240 m may be adequate for small, geometrically simple glaciers, the accuracy is affected by these constraints for glaciers that combine larger spatial extent with strong surface heterogeneity, ultimately leading to greater estimation uncertainty and systematic bias. Millan et al. (2019) reported that the surface velocity of the Mer de Glace averages about 70 m/yr along the lower glacier tongue but rises to over 500 m/yr in the ice fall located below the equilibrium line altitude (ELA). This pronounced spatial variability in flow speed is directly relevant to our results. As shown in Figs. 6 and 7, the largest discrepancies between ITS_LIVE and GNSS velocities in the French Alps are concentrated in precisely these zones — the lower glacier tongue and the ice fall — where steep velocity gradients and complex flow dynamics challenge the feature-tracking algorithm. This spatial correspondence suggests that the velocity errors we observe are not random but are systematically associated with regions of rapid and highly variable ice motion.

Beyond chip size effects, we explored the relationship between ITS_LIVE velocity errors and glacier elevation. Elevation and surface zone represent one of the most important controls on ITS_LIVE accuracy for optical sensors. Above the equilibrium line, fresh snow and firn dominate the surface, producing spectrally homogeneous textures that offer very little contrast for NCC-based feature tracking, degrading the performance of Landsat-8 and Sentinel-2 (Heid and Kaab, 2012). Accumulation-zone points such as Kaskawulsh Upper (1,702 m), Lowell Upper (1,220 m), and Grosser Aletschgletscher (3,329 m) therefore exhibit reduced optical tracking reliability, as reflected in their higher RMSE values in Table 3. In contrast, ablation-zone points — the majority of the Yukon points and the lower-elevation French and Swiss points — have exposed ice with crevasses, debris, and melt features that provide abundant textural contrast, resulting in more reliable NCC tracking. Among the French points, the high-elevation Talèfre point (2,693 m) and the upper Mer de Glace points (above 2,150 m) are expected to show deteriorated optical tracking performance. This is consistent with the Millan (2019) study, which shows that image matching becomes more complex further upstream because of the limited number of surface features and the persistent shadows cast by steep surrounding mountains. In contrast, lower-elevation points (e.g., Mer de Glace Points 1–2 at 1,758–1,978 m) benefit from better surface contrast, although they suffer more from proximity to rock. A comparable elevation-dependent error pattern was reported by Waechter et al. (2015). In their analysis, mean velocity errors were higher for high-elevation and coastal image pairs and lowest for inland pairs covering relatively slow-flowing glaciers. Specifically, errors over bedrock and along ice divides reached 16.58 and 24.89 m/yr, respectively, for 2011 fine-beam imagery, compared with 12.66 and 17.98 m/yr for 2012 ultrafine wide imagery. They attributed this spatial gradient to two main factors: first, steep, heavily glaciated accumulation basins offer few stable, low-motion surfaces suitable as zero-displacement reference points for calibration; and second, fast-flowing glaciers require larger search windows in the matching algorithm, thereby increasing the likelihood of spurious matches. Both mechanisms are relevant to the high-elevation French points discussed above, where limited stable terrain and complex flow dynamics similarly degrade tracking reliability.

Aspect and illumination introduce an additional source of error for optical sensors. In mountainous regions, complex topography and varying solar illumination make optical imagery susceptible to shadow effects (Lacroix et al., 2018 ; Charrier et al., 2026), which reduce surface contrast and compromise feature tracking. Northwest-facing points — specifically Donjek

Upper (348°NW) and Lowell Upper (344°NW) — receive less direct sunlight and are more prone to shadowing, which partly explains their elevated RMSE values (53.9 m/yr and 49.6 m/yr, respectively; Table 3) relative to lower-glacier measurement points. Shadow and snow effects are not independent; both disproportionately affect measurements in upper glacier regions and accumulation zones, and their combined influence is reflected in the consistently higher errors observed at high-elevation, northwest-facing points (Charrier et al., 2026).

Table 3: RMSE of ITS_LIVE Glacier Velocity Estimates

Glacier Point	Glims_ID	Velocity RMSE (m/yr)
Lowell Upper	G221355E60283N	53.9
Kaskawulsh Upper	G220886E60666N	49.6
Kaskawulsh Middle	G220886E60666N	36.7
Lowell Corner	G221355E60283N	36.7
Lowell Middle	G221355E60283N	35.7
Kaskawulsh Lower	G220886E60666N	31.6
Donjek Lower	G220176E60979N	24.4
Donjek Upper	G220176E60979N	23.1
Lowell Lower	G221355E60283N	22.9

Glacier flow dynamics further modulate ITS_LIVE accuracy, as shown in Table 3. Glaciers with relatively stable flow, such as Donjek Glacier, exhibit lower RMSE and smaller deviations between satellite-derived and GNSS velocities. In contrast, glaciers with more complex flow patterns — such as Kaskawulsh and Lowell — show higher RMSE, particularly in regions of rapid flow or surge behavior. This is consistent with the general tendency for larger velocities to be associated with larger absolute errors, as faster-moving surfaces undergo more change between acquisition dates, increasing the difficulty of reliable feature tracking.

6.3 Uncertainty measure

In order to provide an assessment of the errors associated with the product, we evaluate whether the deviation of ITS_LIVE from GNSS measurements is comparable to the uncertainties provided by the ITS_LIVE product. Fig. 9 presents the annual time series of ITS_LIVE *v_error* compared with the GNSS–ITS_LIVE deviation, with no *v_error* thresholding applied. For Sentinel-1 (Fig. 9a), errors are generally low and stable across the time series, with median values mostly below 30 m/yr for both measures. The ITS_LIVE *v_error* tends to be slightly larger than the GNSS–ITS_LIVE deviation, with wider interquartile ranges, while the majority of values remain below 100 m/yr with occasional outliers reaching up to 250 m/yr. Lei et al. (2022) assessed ITS_LIVE Sentinel-1 velocities at three globally representative sites (Jakobshavn Isbræ in Greenland, Pine Island Glacier in Antarctica, and Malaspina Glacier in Alaska), reporting an average uncertainty of 61 m/yr, with errors of 35 m/yr in vx and 71 m/yr in vy. The higher *vy error* reflects the coarser resolution in the radar azimuth direction. This uncertainty value is consistent with the results of our study. For Sentinel-2 (Fig. 9b), error magnitudes are generally lower than those of Sentinel-1, with medians mostly below 20 m/yr. The GNSS–ITS_LIVE deviation was larger than the ITS_LIVE *v_error* from 2018–2022, with GNSS–ITS_LIVE medians typically ranging from 5–10 m/yr and *v_error* medians remaining consistently lower at roughly 2–5 m/yr. For Landsat-8 (Fig. 9c), both measures are broadly consistent, though the spread is considerably larger than for the other two sensors, with median values generally below 50 m/yr but with outliers reaching up to 400 m/yr, particularly in earlier years (2013–2015), likely reflecting fewer available image pairs or lower image quality in the early Landsat-8 record. Discrepancies between these two uncertainty measures are attributed to several reasons: 1) *v_error* from the ITS_LIVE product is first estimated over stable surfaces with the error later translated to each spatial location while the deviation between GNSS measurement and ITS_LIVE velocity gives a measure of the localized error. As noted by Zheng et al. (2023), the GNSS and ITS_LIVE deviation arises because correctly matched features on the glacier surface follow a different noise distribution than those on stable terrain, likely owing to differences in local surface roughness (topography) and texture (reflectance) between ice and ice-free areas. 2) given a chip size of 240 m, high-resolution satellite imagery (Sentinel-2) is able to resolve more surface features in the NCC in comparison with Landsat-8, leading to a high Signal-to-Noise Ratio (SNR) over stable surfaces and thus a lower *v_error* estimate. In general, the two uncertainty measures show broadly comparable magnitudes across all three sensors, suggesting that the ITS_LIVE *v_error* is a reasonable indicator of product uncertainty.

Since the NCC method generally derives velocity from displacement, we also evaluate the displacement uncertainty across the three sensors. Fig. 10 shows the displacement uncertainty (in meters) associated with each sensor. For Landsat-8 and Sentinel-2, uncertainty increases with the image-pair time interval, consistent with greater temporal decorrelation over longer baselines. Note that greater displacement uncertainty does not necessarily translate to greater velocity error, as displacement error must be divided by the time separation to obtain velocity error. For temporal baselines exceeding 60 days, glacier surfaces undergo more changes due to melting, snow accumulation, crevassing, and deformation. A similar conclusion was reached by Millan et al., who found that capturing velocity fluctuations of about 10 m/yr requires repeat cycles longer than 60 days (Millan et al., 2019). Temporal decorrelation makes it harder to accurately track the same surface features (Gardner et al., 2025), as these processes progressively alter the glacier surface. Within a 60-day interval, the uncertainties for Sentinel-1, Sentinel-2, and Landsat-8 are similarly low, generally below 10 meters. Since displacement error over a 60-day temporal baseline can be considered approximately constant, the velocity error (i.e., displacement error divided by temporal baseline) decreases as the temporal baseline increases. Sentinel-1 is more prone to temporal decorrelation for temporal baselines exceeding 60 days.

The ITS_LIVE *v_error* for the annual composite product is generally lower than the GNSS–ITS_LIVE deviation (Fig. 11). The GNSS–ITS_LIVE deviation includes seasonal variations of uncertainty when calculating the errors, while the ITS_LIVE *v_error* accounts for typical seasonal velocity variability using a mathematical best fit (Gardner et al., 2025).

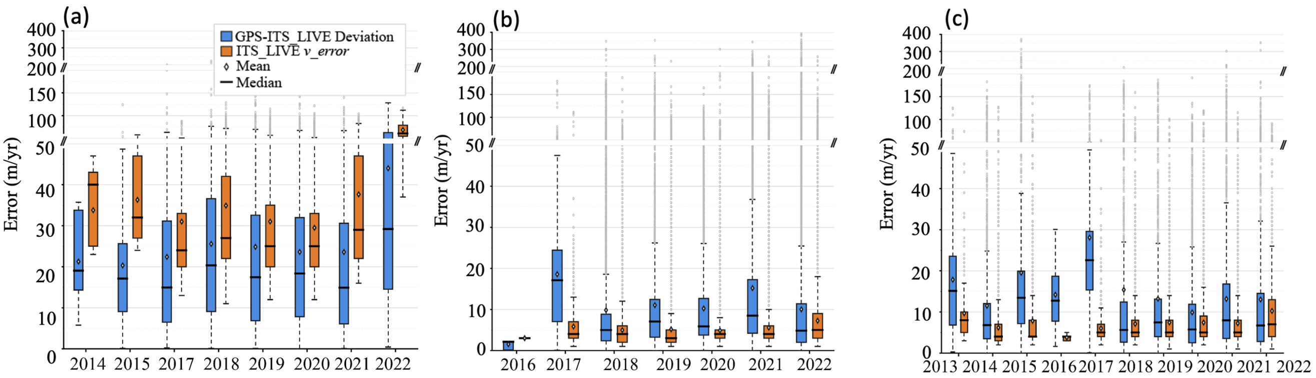

Figure 9: Yearly comparison of uncertainty measures (GNSS–ITS_LIVE deviation and ITS_LIVE *v_error* product) in Yukon: (a) Sentinel-1, (b) Sentinel-2, and (c) Landsat-8.

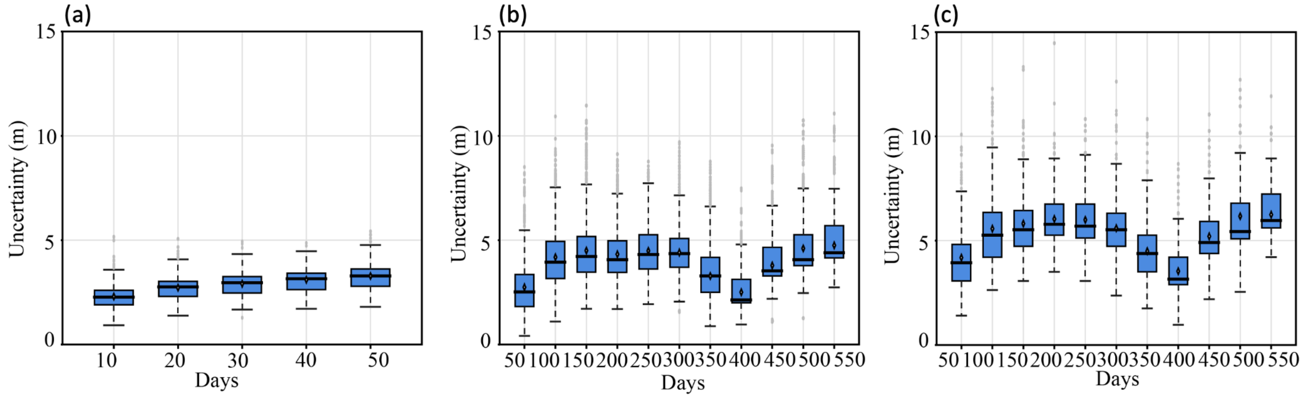

Figure 10: Displacement uncertainty versus time interval: (a) Sentinel-1, (b) Sentinel-2, and (c) Landsat-8.

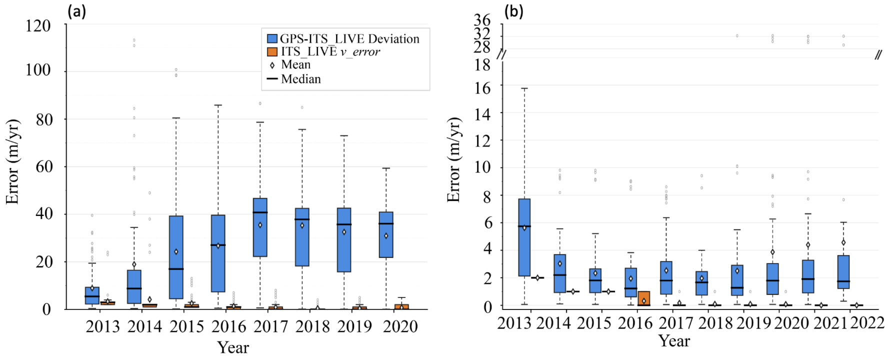

Figure 11: Annual comparison of uncertainty measures (GNSS–ITS_LIVE deviation and ITS_LIVE annual composite *v_error*): (a) France, (b) Switzerland.

7 Conclusions

This study systematically evaluates the accuracy of ITS_LIVE velocity estimates in comparison to GNSS-derived velocity measurements for glaciers in mountainous regions. Our analysis covers three regions — the Yukon for dense time-series comparisons, and France and Switzerland for annual-interval comparisons. For the dense time-series GNSS data in the Yukon region, we applied two outlier removal strategies to the ITS_LIVE data to improve accuracy: error thresholding and spatial filtering. Accuracy is assessed across different satellites (both radar and optical sensors) and diverse mountain glacier regimes by considering glacier-wide characteristics, topography, and accumulation/ablation zones. We analyze GNSS variability and its agreement with ITS_LIVE products to identify conditions under which the datasets perform best and to quantify limitations related to spatial and temporal resolution.

In the Yukon region, the Sentinel-1 *vy* component (RMSE 9.4 m/yr, bias −1.7 m/yr) outperformed the *vx* component (RMSE 23.1 m/yr, bias 0.8 m/yr), reflecting the higher precision of Sentinel-1 in the range direction. For optical sensors, both Landsat-8 and Sentinel-2 compared well with GNSS velocities. Landsat-8 exhibited a lower RMSE (16.3 m/yr) and NMAD (4.3 m/yr) but a higher bias (3.7 m/yr), while Sentinel-2 showed a higher RMSE (22.4 m/yr) and NMAD (9.6 m/yr) but negligible bias (−0.1 m/yr). Both optical sensors successfully captured the 2022 glacier surge event with velocities exceeding 500 m/yr, demonstrating the capability of ITS_LIVE products to detect dynamic glacier flow events; notably, Sentinel-2's shorter time interval enabled the resolution of finer surface features.

For annual interval comparisons in Switzerland and France, ITS_LIVE products perform considerably better over Swiss glaciers than French ones. Simple annual averages of ITS_LIVE image-pair products show much better agreement with GNSS measurements in Switzerland (RMSE 11.5–19.4 m/yr) than in France (RMSE 40.9–55.2 m/yr). The ITS_LIVE annual composite product further improves accuracy, achieving lower biases than simple annual averages in both regions (−1.2 m/yr in Switzerland and −28.9 m/yr in France), suggesting that the error-weighted least-squares fitting approach partially mitigates systematic biases present in individual image-pair averages.

The ITS_LIVE *v_error* product provides a reasonable indicator of uncertainty, with magnitudes broadly comparable to the GNSS–ITS_LIVE deviation across all three sensors. For Sentinel-1, both types of errors are low and stable with median values below 25 m/yr. Sentinel-2 *v_error* shows the lowest error magnitudes with medians below 20 m/yr, though the GNSS–ITS_LIVE deviation consistently exceeds the *v_error* estimate; this is attributable to Sentinel-2's higher spatial resolution, which improves the SNR over stable surfaces and thus reduces the estimated *v_error*. Landsat-8 exhibits the largest spread, with outliers reaching up to 400 m/yr, particularly in earlier years. For optical sensors, displacement uncertainty increases with time interval due to temporal decorrelation, though within a 60-day baseline all three sensors show similarly low uncertainties below 10 meters. For the annual composite product, the ITS_LIVE *v_error* is generally lower than the GNSS–ITS_LIVE deviation, as the latter captures seasonal variations in uncertainty that the *v_error* product accounts for through a mathematical best fit.

Based on these results, we provide practical guidance for reliable use of ITS_LIVE v2 in alpine glaciology and validation while acknowledging its constraints. Overall, the ITS_LIVE data provides a valuable source for glacier velocity estimation, with strong agreement to GNSS data, especially for larger glaciers where search chips do not overlap ice free terrain. Future work should expand the GNSS validation network to a broader range of glacier types, sizes, and climatic settings to further refine the error characterization presented here. In addition, algorithmic improvements such as adaptive chip-size optimisation and improved glacier boundary masking could help reduce velocity underestimation near glacier margins, while machine-learning-based filtering methods may offer enhanced noise removal for glaciers with complex geometries.

Author contributions

J.Z. and L.Y. designed the study. L.Y. supervised the study. J.Z. developed the methodology, processed the data, and analyzed the results, with feedback from L.Y., A.G., A.D., and L.C. L.C. and C.D. provided the GNSS data for the Yukon region. A.D. and L.C. provided the GNSS data for France and Switzerland. J.Z. led the writing of the manuscript, and all authors contributed to and approved the final version.

Acknowledgement

This work was financially supported by the Ministry of Science and Technology through the National Key R&D Program of China under grant number 2022YFB3903300 and grant number 2022YFB3903301. A.G.’s contributions were carried out at the Jet Propulsion Laboratory, California Institute of Technology, under a contract with the National Aeronautics and Space Administration (80NM0018D0004). LC acknowledges support from the Centre National d'Etudes Spatiales for her postdoctoral fellowship. AD and LC acknowledge support from the French Programme National de Télédétection Spatiale (PNTS). We extend our gratitude to Luke Copland and Christine Dow for providing the GNSS datasets from the Yukon, Canada region through collaboration. Luke Copland and Christine Dow thank the Natural Sciences and Engineering Research Council of Canada, Polar Continental Shelf Program, Canada Foundation for Innovation, Ontario Research Fund, and New Frontiers Research Fund for funding to purchase and operate the Yukon GNSS stations, and the staff of Kluane Lake Research Station and graduate students from University of Ottawa and University of Waterloo for assistance and support in the field.

Data availability

ITS_LIVE data are publicly available at https://its-live.jpl.nasa.gov/. In Switzerland, the Global Navigation Satellite System data provided by the Swiss Glacier Monitoring Network (GLAMOS) are freely accessible at https://www.glamos.ch. In France, in situ differential Global Navigation Satellite System measurements were obtained from the glacier observatory

GLACIOCLIM, which provides multidecadal observations in the French Alps, including Argentière Glacier and Mer de Glace; these data are available at https://glacioclim.osug.fr/Donnees-des-Alpes.

Competing interests

The authors declare no competing interest.

References

Abe, T., Furuya, M., and Sakakibara, D.: Brief communication: Twelve-year cyclic surging episodes at Donjek Glacier in Yukon, Canada, The Cryosphere, 10, 1427–1432, https://doi.org/10.5194/tc-10-1427-2016, 2016.

Banerjee, D., Lilien, D. A., Truffer, M., Luckman, A., Wild, C. T., Pettit, E. C., Scambos, T. A., Muto, A., and Alley, K. E.: Evolution of shear-zone fractures presages the disintegration of Thwaites Eastern Ice Shelf, J. Geophys. Res.-Earth, 130, https://doi.org/10.1029/2025jf008352, 2025.

Bauder, A., Funk, M., and Huss, M.: Ice-volume changes of selected glaciers in the Swiss Alps since the end of the 19th century, Ann. Glaciol., 46, 145–149, https://doi.org/10.3189/172756407782871701, 2007.

Bevington, A. and Copland, L.: Characteristics of the last five surges of Lowell Glacier, Yukon, Canada, since 1948, J. Glaciol., 60, 113–123, https://doi.org/10.3189/2014JoG13J134, 2014.

Bhambri, R., Hewitt, K., Kawishwar, P., and Pratap, B.: Surge-type and surge-modified glaciers in the Karakoram, Sci. Rep., 7, 15391, https://doi.org/10.1038/s41598-017-15473-8, 2017.

Breunig, M. M., Kriegel, H.-P., Ng, R. T., and Sander, J.: LOF: Identifying density-based local outliers, in: Proceedings of the 2000 ACM SIGMOD International Conference on Management of Data, 93–104, https://doi.org/10.1145/342009.335388, 2000.

Charrier, L., Dehecq, A., Guo, L., Brun, F., Millan, R., Lioret, N., Copland, L., Maier, N., Dow, C., and Halas, P.: TICOI: An operational Python package to generate regularized glacier velocity time series, The Cryosphere, 19, 4555–4583, https://doi.org/10.5194/tc-19-4555-2025, 2025.

Charrier, L., Lioret, N., Brun, F., Dehecq, A., Millan, R., Togaibekov, A., Walpersdorf, A., Cusicanqui, D., and Rabatel, A.: Seasonal biases in glacier surface flow velocities measured from optical remote sensing images, EGUsphere [preprint], https://doi.org/10.5194/egusphere-2026-946, 2026.

Cuffey, K. M. and Paterson, W. S. B.: The Physics of Glaciers, 4th edn., Elsevier, Amsterdam, 2010.

Fahnestock, M., Scambos, T., Moon, T., Gardner, A., Haran, T., and Klinger, M.: Rapid large-area mapping of ice flow using Landsat 8, Remote Sens. Environ., 185, 84–94, https://doi.org/10.1016/j.rse.2015.11.023, 2016.

Flowers, G. E., Copland, L., and Schoof, C. G.: Contemporary glacier processes and global change: Recent observations from Kaskawulsh Glacier and the Donjek Range, St. Elias Mountains, Arctic, 67, 22–34, https://doi.org/10.14430/arctic4356, 2014.

Friedl, P., Seehaus, T., and Braun, M.: Global time series and temporal mosaics of glacier surface velocities derived from Sentinel-1 data, Earth Syst. Sci. Data, 13, 4653–4675, https://doi.org/10.5194/essd-13-4653-2021, 2021.

Gardner, A. S., Moholdt, G., Scambos, T., Fahnestock, M., Ligtenberg, S., Van Den Broeke, M., and Nilsson, J.: Increased West Antarctic and unchanged East Antarctic ice discharge over the last 7 years, The Cryosphere, 12, 521–547, https://doi.org/10.5194/tc-12-521-2018, 2018.

Gardner, A. S., Greene, C. A., Kennedy, J. H., Fahnestock, M. A., Liukis, M., López, L. A., Lei, Y., Scambos, T. A., and Dehecq, A.: ITS_LIVE global glacier velocity data in near-real time, The Cryosphere, 19, 3517–3533, https://doi.org/10.5194/tc-19-3517-2025, 2025.

GLACIOCLIM: Glacier observatory data for the French Alps, available at: https://glacioclim.osug.fr/Mer-de-Glace (last access: April 2026).

GLAMOS (2022). Swiss Glacier Flow Velocity, release 2022, Glacier Monitoring Switzerland, doi:10.18750/flowvelocity.2022.r2022.

Greene, C. A., Gardner, A. S., and Andrews, L. C.: Detecting seasonal ice dynamics in satellite images, The Cryosphere, 14, 4365–4378, https://doi.org/10.5194/tc-14-4365-2020, 2020.

Greene, C. A., Gardner, A. S., Schlegel, N. J., and Fraser, A. D.: Antarctic calving loss rivals ice-shelf thinning, Nature, 609, 948–953, https://doi.org/10.1038/s41586-022-05037-w, 2022.

Gupta, H. V., Kling, H., Yilmaz, K. K., and Martinez, G. F.: Decomposition of the mean squared error and NSE performance criteria: Implications for improving hydrological modelling, J. Hydrol., 377, 80–91, https://doi.org/10.1016/j.jhydrol.2009.08.003, 2009.

Heid, T. and Kääb, A.: Evaluation of existing image matching methods for deriving glacier surface displacements globally from optical satellite imagery, Remote Sens. Environ., 118, 339–355, https://doi.org/10.1016/j.rse.2011.11.024, 2012.

Herreid, S. and Truffer, M.: Automated detection of unstable glacier flow and a spectrum of speedup behavior in the Alaska Range, J. Geophys. Res.-Earth, 121, 64–81, https://doi.org/10.1002/2015jf003502, 2016.

Hock, R., Bliss, A., Marzeion, B., Giesen, R. H., Hirabayashi, Y., Huss, M., Radić, V., and Slangen, A. B. A.: GlacierMIP – A model intercomparison of global-scale glacier mass-balance models and projections, J. Glaciol., 65, 453–467, https://doi.org/10.1017/jog.2019.22, 2019.

Huss, M., Dhulst, L., and Bauder, A.: New long-term mass-balance series for the Swiss Alps, J. Glaciol., 61, 551–562, https://doi.org/10.3189/2015JoG15J015, 2015.

ITS_LIVE: Regional glacier and ice sheet surface velocities, available at: http://its-live-data.jpl.nasa.gov.s3.amazonaws.com/documentation/ITS_LIVE-Regional-Glacier-and-Ice-Sheet-Surface-Velocities.pdf (last access: April 2026).

Johnson, P.: A possible advanced hypsithermal position of the Donjek Glacier, Arctic, 25, 302–305, 1972a.

Johnson, P.: The morphological effects of surges of the Donjek Glacier, St Elias Mountains, Yukon Territory, Canada, J. Glaciol., 11, 227–234, 1972b.

Joughin, I., Smith, B. E., Howat, I. M., Scambos, T., and Moon, T.: Greenland flow variability from ice-sheet-wide velocity mapping, J. Glaciol., 56, 415–430, 2010.

Joughin, I., Smith, B. E., and Howat, I.: Greenland Ice Mapping Project: Ice flow velocity variation at sub-monthly to decadal timescales, The Cryosphere, 12, 2211–2227, https://doi.org/10.5194/tc-12-2211-2018, 2018.

Kääb, A., Winsvold, S. H., Altena, B., Nuth, C., Nagler, T., and Wuite, J.: Glacier remote sensing using Sentinel-2. Part I: Radiometric and geometric performance, and application to ice velocity, Remote Sens., 8, 598, https://doi.org/10.3390/rs8070598, 2016.

Kelly, J. T., Hehlen, M., and McGee, S.: Uncertainty of satellite-derived glacier flow velocities in a temperate alpine setting (Juneau Icefield, Alaska), Remote Sens., 15, 3828, https://doi.org/10.3390/rs15153828, 2023.

Kochtitzky, W., Copland, L., Painter, M., and Dow, C.: Draining and filling of ice-dammed lakes at the terminus of surge-type Dań Zhùr (Donjek) Glacier, Yukon, Canada, Can. J. Earth Sci., 57, 1337–1348, https://doi.org/10.1139/cjes-2019-0233, 2020.

Lacroix, P., Bièvre, G., Pathier, E., Kniess, U., and Jongmans, D.: Use of Sentinel-2 images for the detection of precursory motions before landslide failures, Remote Sens. Environ., 215, 507–516, https://doi.org/10.1016/j.rse.2018.03.042, 2018.

Lei, Y., Gardner, A., and Agram, P.: Autonomous Repeat Image Feature Tracking (autoRIFT) and its application for tracking ice displacement, Remote Sens., 13, 749, https://doi.org/10.3390/rs13040749, 2021.

Lei, Y., Gardner, A. S., and Agram, P.: Processing methodology for the ITS_LIVE Sentinel-1 ice velocity products, Earth Syst. Sci. Data, 14, 5111–5137, https://doi.org/10.5194/essd-14-5111-2022, 2022.

Liu, J., Gendreau, M., Enderlin, E. M., and Aberle, R.: Improved records of glacier flow instabilities using customized NASA autoRIFT (CautoRIFT) applied to PlanetScope imagery, The Cryosphere, 18, 3571–3590, https://doi.org/10.5194/tc-18-3571-2024, 2024.

Lopez-Saez, J., Corona, C., Slamova, L., Huss, M., Daux, V., Nicolussi, K., and Stoffel, M.: Multiproxy tree ring reconstruction of glacier mass balance: Insights from Pinus cembra trees growing near Silvretta Glacier (Swiss Alps), Clim. Past, 20, 1251–1267, https://doi.org/10.5194/cp-20-1251-2024, 2024.

Meier, M. F., Dyurgerov, M. B., Rick, U. K., O'Neel, S., Pfeffer, W. T., Anderson, R. S., Anderson, S. P., and Glazovsky, A. F.: Glaciers dominate eustatic sea-level rise in the 21st century, Science, 317, 1064–1067, https://doi.org/10.1126/science.1143906, 2007.

Millan, R., Mouginot, J., Rabatel, A., Jeong, S., Cusicanqui, D., Derkacheva, A., and Chekki, M.: Mapping surface flow velocity of glaciers at regional scale using a multiple sensors approach, Remote Sens., 11, 2498, https://doi.org/10.3390/rs11212498, 2019.

Millan, R., Mouginot, J., Rabatel, A., and Morlighem, M.: Ice velocity and thickness of the world's glaciers, Nat. Geosci., 15, 124–129, https://doi.org/10.1038/s41561-021-00885-z, 2022.

Minchew, B. M., Simons, M., Riel, B., and Milillo, P.: Tidally induced variations in vertical and horizontal motion on Rutford Ice Stream, West Antarctica, inferred from remotely sensed observations, J. Geophys. Res.-Earth, 122, 167–190, https://doi.org/10.1002/2016JF003971, 2017.

Mouginot, J., Rignot, E., Scheuchl, B., and Millan, R.: Comprehensive annual ice sheet velocity mapping using Landsat-8, Sentinel-1, and RADARSAT-2 data, Remote Sens., 9, 364, https://doi.org/10.3390/rs9040364, 2017.

Nagler, T., Rott, H., Hetzenecker, M., Wuite, J., and Potin, P.: The Sentinel-1 mission: New opportunities for ice sheet observations, Remote Sens., 7, 9371–9389, https://doi.org/10.3390/rs70709371, 2015.

Peyaud, V., Bouchayer, C., Gagliardini, O., Vincent, C., Gillet-Chaulet, F., Six, D., and Laarman, O.: Numerical modeling of the dynamics of the Mer de Glace glacier, French Alps: Comparison with past observations and forecasting of near-future evolution, The Cryosphere, 14, 3979–3994, https://doi.org/10.5194/tc-14-3979-2020, 2020.

Pfeffer, W. T., Arendt, A. A., Bliss, A., Bolch, T., Cogley, J. G., Gardner, A. S., Hagen, J. O., Hock, R., Kaser, G., Kienholz, C., Miles, E. S., Moholdt, G., Mölg, N., Paul, F., Radić, V., Rastner, P., Raup, B. H., Rich, J., Sharp, M. J., and the Randolph Consortium: The Randolph Glacier Inventory: A globally complete inventory of glaciers, J. Glaciol., 60, 537–552, https://doi.org/10.3189/2014JoG13J176, 2014.

Rabatel, A., Sanchez, O., Vincent, C., and Six, D.: Estimation of glacier thickness from surface mass balance and ice flow velocities: A case study on Argentière Glacier, France, Front. Earth Sci., 6, 112, https://doi.org/10.3389/feart.2018.00112, 2018.

Rabatel, A., Ducasse, E., Millan, R., and Mouginot, J.: Satellite-derived annual glacier surface flow velocity products for the European Alps, 2015–2021, Data, 8, 66, https://doi.org/10.3390/data8040066, 2023.

Radić, V., Bliss, A., Beedlow, A. C., Hock, R., Miles, E., and Cogley, J. G.: Regional and global projections of twenty-first century glacier mass changes in response to climate scenarios from global climate models, Clim. Dynam., 42, 37–58, https://doi.org/10.1007/s00382-013-1719-7, 2014.

Rousseeuw, P. J. and Croux, C.: Alternatives to the median absolute deviation, J. Am. Stat. Assoc., 88, 1273–1283, https://doi.org/10.1080/01621459.1993.10476408, 1993.

Sevestre, H. and Benn, D. I.: Climatic and geometric controls on the global distribution of surge-type glaciers: Implications for a unifying model of surging, J. Glaciol., 61, 646–662, https://doi.org/10.3189/2015JoG14J136, 2015.

Solgaard, A., Kusk, A., Merryman Boncori, J. P., Dall, J., Mankoff, K. D., Ahlstrøm, A. P., Andersen, S. B., Citterio, M., Karlsson, N. B., Kjeldsen, K. K., Korsgaard, N. J., Larsen, S. H., and Fausto, R. S.: Greenland ice velocity maps from the PROMICE project, Earth Syst. Sci. Data, 13, 3491–3512, https://doi.org/10.5194/essd-13-3491-2021, 2021.

Stringer, C. D., Macfee, M. W., Carrivick, J. L., Láska, K., Engel, Z., Matějka, M., Harpur, C., Nývlt, D., Quincey, D. J., and Davies, B. J.: Accelerated glacier changes on the James Ross Archipelago, Antarctica, from 2010 to 2023, J. Glaciol., 1–32, https://doi.org/10.1017/jog.2025.10075, 2025.

Troilo, F., Dematteis, N., Zucca, F., Funk, M., and Giordan, D.: Monthly velocity and seasonal variations of the Mont Blanc glaciers derived from Sentinel-2 between 2016 and 2024, The Cryosphere, 18, 3891–3909, https://doi.org/10.5194/tc-18-3891-2024, 2024.

Van Wychen, W., Courtney, B., Luke, C., Erika, B., and Dow, C.: RADARSAT Constellation Mission derived winter glacier velocities for the St. Elias Icefield, Yukon/Alaska: 2022 and 2023, Can. J. Remote Sens., 49, 2264395, https://doi.org/10.1080/07038992.2023.2264395, 2023.

Van Wychen, W., Jiskoot, H., Shannon, K., and Gorwill, C.: The long multiphase trunk-tributary surge history of the high-Arctic Chapman Glacier, 1959–2023, Arct. Antarct. Alp. Res., 57, 2441541, https://doi.org/10.1080/15230430.2024.2441541, 2025.

Vincent, C., Gilbert, A., Walpersdorf, A., Gimbert, F., Gagliardini, O., Jourdain, B., Roldan Blasco, J. P., Laarman, O., Piard, L., Six, D., Moreau, L., Cusicanqui, D., and Thibert, E.: Evidence of seasonal uplift in the Argentière Glacier (Mont Blanc area, France), J. Geophys. Res.-Earth, 127, e2021JF006454, https://doi.org/10.1029/2021jf006454, 2022.Waechter, A., Copland, L., and Herdes, E.: Modern glacier velocities across the Icefield Ranges, St Elias Mountains, and variability at selected glaciers from 1959 to 2012, J. Glaciol., 61, 624–634, https://doi.org/10.3189/2015JoG14J147, 2015.

Walden, J., Jacquemart, M., Higman, B., Hugonnet, R., Manconi, A., and Farinotti, D.: Landslide activation during deglaciation in a fjord-dominated landscape: Observations from southern Alaska (1984–2022), Nat. Hazards Earth Syst. Sci., 25, 2045–2073, https://doi.org/10.5194/nhess-25-2045-2025, 2025.

Westerweel, J. and Scarano, F.: Universal outlier detection for PIV data, Exp. Fluids, 39, 1096–1100, https://doi.org/10.1007/s00348-005-0016-6, 2005.

Yang, Z., Chen, Z., Li, G., Mao, Y., Feng, X., and Cheng, X.: Comparison of the precision of glacier flow rates derived from offset-tracking using Sentinel-2 and Landsat-8/9 imagery, Adv. Polar Sci., 35, 238–251, 2024.

Young, E. M., Flowers, G. E., Berthier, E., and Latto, R.: An imbalancing act: The delayed dynamic response of the Kaskawulsh Glacier to sustained mass loss, J. Glaciol., 67, 313–330, https://doi.org/10.1017/jog.2020.107, 2021.

Zemp, M., Huss, M., Thibert, E., Eckert, N., McNabb, R., Huber, J., Barandun, M., Machguth, H., Nussbaumer, S. U., Gärtner-Roer, I., Thomson, L., Paul, F., Maussion, F., Kutuzov, S., and Cogley, J. G.: Global glacier mass changes and their contributions to sea-level rise from 1961 to 2016, Nature, 568, 382–386, https://doi.org/10.1038/s41586-019-1071-0, 2019.

Zhang, J., Jia, L., Menenti, M., and Ren, S.: Interannual and seasonal variability of glacier surface velocity in the Parlung Zangbo Basin, Tibetan Plateau, Remote Sens., 13, 80, https://doi.org/10.3390/rs13010080, 2021.

Zhang, J., Lei, Y., Charrier, L., Dehecq, A., and Gardner, A. S.: Validation of the surface velocity field of mountain glaciers from ITS_LIVE v2 with in situ GPS data, in: IGARSS 2024 – 2024 IEEE International Geoscience and Remote Sensing Symposium, 7–12 July 2024, 9–13, https://doi.org/10.1109/IGARSS53475.2024.10642917, 2024.

Zheng, W., Bhushan, S., Van Wyk de Vries, M., Kochtitzky, W., Shean, D., Copland, L., Dow, C., Jones-Ivey, R., and Pérez, F.: GLAcier Feature Tracking testkit (GLAFT): a statistically and physically based framework for evaluating glacier velocity products derived from optical satellite image feature tracking, The Cryosphere, 17, 4063–4078, https://doi.org/10.5194/tc-17-4063-2023, 2023.

Zhou, Y., Li, X., Zheng, D., and Li, Z.: Evolution of geodetic mass balance over the largest lake-terminating glacier in the Tibetan Plateau with a revised radar penetration depth based on multi-source high-resolution satellite data, Remote Sens. Environ., 275, 113029, https://doi.org/10.1016/j.rse.2022.113029, 2022.